NTNU – Trondheim
Norwegian University of
Science and Technology

Numerical Simulation of Flow Around Remotely Operated Vehicle (ROV)

Steinar Skorpa

Marine Technology
Submission date: June 2012
Supervisor: Dag Myrhaug, IMT
Co-supervisor: Muk Chen Ong, IMT
Audun Kristoffersen, IKM Ocean Design

Norwegian University of Science and Technology
Department of Marine Technology

NTNU Trondheim
Norwegian University of Science and Technology
Department of Marine Technology

MASTER THESIS IN MARINE TECHNOLOGY

SPRING 2012

FOR

STUD. TECHN. STEINAR SKORPA

NUMERICAL SIMULATION OF FLOW AROUND REMOTELY OPERATED VEHICLE (ROV)

ROVs are frequently used in marine operations and an important issue related to the design is the stability of the ROV in survey-mode, i.e. operating at a constant speed.

The purpose of this study is to use numerical flow simulations in order to study the detailed flow structure around the ROV in order to learn how to achieve a stable ROV in survey-mode.

The student shall:

1. Give a background of ROV.
2. Simplify the ROV for flow modeling purposes.
3. Describe the computational tools ANSYS FLUENT.
4. Give a background description of turbulence modeling.
5. Perform numerical simulations of the flow around simplified shapes of ROVs.
6. Discuss consequences of flow structure for the stability of ROVs.

In the thesis the candidate shall present his personal contribution to the resolution of problem within the scope of the thesis work.

Theories and conclusions should be based on mathematical derivations and/or logic reasoning identifying the various steps in the deduction.

The candidate should utilize the existing possibilities for obtaining relevant literature.

The thesis should be organized in a rational manner to give a clear exposition of results, assessments, and conclusions. The text should be brief and to the point, with a clear language. Telegraphic language should be avoided.

The thesis shall contain the following elements: A text defining the scope, preface, list of contents, summary, main body of thesis, conclusions with recommendations for further work, list of symbols and acronyms, reference and (optional) appendices. All figures, tables and equations shall be numerated.

The supervisor may require that the candidate, in an early stage of the work, present a written plan for the completion of the work. The plan should include a budget for the use of computer and laboratory resources that will be charged to the department. Overruns shall be reported to the supervisor.

The original contribution of the candidate and material taken from other sources shall be clearly defined. Work from other sources shall be properly referenced using an acknowledged referencing system.

NTNU Trondheim
Norwegian University of Science and Technology
Department of Marine Technology

The thesis shall be submitted in two copies:

- Signed by the candidate
- The text defining the scope included
- In bound volume(s)
- Drawings and/or computer prints that cannot be bound should be organized in a separate folder.
- The bound volume shall be accompanied by a CD or DVD containing the written thesis in Word or PDF format. In case computer programs have been made as part of the thesis work, the source code shall be included. In case of experimental work, the experimental results shall be included in a suitable electronic format.

Contact : IKM Ocean Design, Audun Schanche Kristoffersen
Advisors : Dr. Muk Chen Ong
: Professor Dag Myrhaug

Deadline : 10.06.2012

Dag Myrhaug
Supervisor

Preface

This report is the result of the Master's Thesis (TMR4900) in Marine Technology at the Norwegian University of Science and Technology (NTNU), spring 2012. The Master's Thesis counts as 30 ECTS ("Studiepoeng").

The thesis covers flow around 3D bluff bodies; two rectangular cubes and a simplified model of an ROV. The title of the Master's Thesis is "Numerical Simulation of Flow Around Remotely Operated Vehicle (ROV)".

I would like to thank my advisors; Professor Dag Myrhaug (Supervisor) and Dr. Muk Chen Ong. Especially Muk Chen have been of great help whenever I have been in need of guidance. I would also like to thank IKM Ocean Design and IKM Subsea for the opportunity to investigate this highly interesting topic.

Finally, I would also like to thank Professor Sverre Steen for the opportunity to run the final cases on "Kongull", this was of great importance for my Master's Thesis.

Trondheim, June 7th 2012

Steinar Skorpa

Summary

Computational Fluid Dynamics (CFD) have been applied for numerical simulations of the flow around simplified shapes of a Remotely Operated Vehicle (ROV). The simulations have been carried out at $Re = 8.5 \times 10^5$, which coincides with a free stream velocity of one knot in seawater conditions. Detached Eddy Simulation (DES) have been used with the $k - \omega$ SST turbulence model in the near-wall (unsteady RANS) regions. The CFD code FLUENT from ANSYS Inc. have been used.

The first case to be investigated, was a fully submerged rectangular stationary cube with both sharp and rounded edges. The sharp edged case showed good agreement with published reference values. The results for the refined mesh gave $\overline{C_D} = 0.8192$, $C_{Lrms} = 0.0473$ and $St = 0.1132$. The Strouhal number was identical for both meshes, while small discrepancies were seen on the mean drag and the root mean square lift coefficient. For the round edged case, the mean drag coefficient was shown to be about 25% of the sharp edged case ($\overline{C_D} = 0.2257$). The lift was more difficult to model correct and large discrepancies were seen both on the Strouhal number and the root mean square lift coefficient. It was concluded that longer time series were needed in addition to further mesh refinement in order to get more stable mean quantities of the lift history. Some effort were also made on trying the realizable $k - \varepsilon$ turbulence model in the near-wall regions for the round edged case, but without noticeably effect on the results. For both the sharp edged case and the round edged case it was concluded that although the drag was successfully modeled, a further mesh refinement was needed in order to ensure converged results.

For the case of the simplified model of the ROV, three meshes were used for the grid convergence study. Small discrepancies were seen, between 2% and 6.2%. The pitch moment through the Center of Gravity (COG) was also measured and a negative mean value of $\overline{C_M} = -0.2563$ was obtained.

This means that the reported instability for the ROV was also seen in the simplified model. Through a more detailed study of the pressure and velocity distributions, the main problem regions were identified to be above the forward top and below the aft bottom. Here high-velocity regions generate low-pressure regions, which coincides with a negative pitch moment. One proposed solution was the removal of the plate in the aft which span the width of the ROV. The effect of this solution was however found to be questionable. This is due to the components which are placed in front of the plate, and these may actually cause the same effect. For this reason, these components should be relocated.

It was concluded that there should be performed numerical simulations without the plate and the components in front included. The effect of these components could then be studied and a decision on whether to remove the plate could be made. Also, numerical simulations where different locations for the components in front of the plate are tried should be an interesting case to run with respect to the stability analysis.

Sammendrag

"Computational Fluid Dynamics" (CFD) har blitt brukt til å gjøre numeriske analyser av strømningen rundt forenklede modeller av en ROV (Remotely Operated Vehicle). Simuleringene har blitt gjennomført ved et Reynoldstall på $Re = 8.5 \times 10^5$. Dette tilsvarer en strømningshastighet på en knop i sjøvann. "Detached Eddy Simulation" (DES) har blitt benyttet sammen med turbulensmodellen $k - \omega$ SST i områdene nær ROVen. Simuleringene er utført med CFD koden FLUENT fra ANSYS Inc.

De første numeriske analysene ble gjort for en helt neddykket stasjonær rektangulær kube, med både skarpe og avrundede hjørner og kanter. Tilfellet med skarpe kanter viste gode resultater sammenlignet med andre publiserte resultater. Resultatene for det fineste rutenettet (mesh) gav $\overline{C_D} = 0.8192$, $C_{Lrms} = 0.0473$ og $St = 0.1132$. Strouhalstallet var likt for begge rutenettene, mens små avvik ble registrert for motstandskoeffisienten og den kvadratiske middelverdien av løftkoeffisienten. For tilfellet med avrundede kanter og hjørner ble motstandskoeffisienten vist å være kun 25% av det som var tilfellet med skarpe kanter ($\overline{C_D} = 0.2257$). Løftet viste seg å være vanskeligere å modellere korrekt, og store avvik i både Strouhalstall og i den kvadratiske middelverdien ble registrert. Det ble konkludert at det trengtes både lengre tidsserier og finjustering av rutenett for å kunne oppnå stabile middelverdier av løftet. Det ble også forsøkt å benytte turbulensmodellen $k - \varepsilon$ nær ROVen, men dette var uten nevneverdige påvirkninger på resultatet. Til slutt ble det konkludert med at selv om motstanden var bra modellert for begge tilfeller, ville det trenges videre finjustering av rutenett for å kunne se konvergens.

For tilfellet med den forenklede modellen av ROVen ble det laget tre forskjellige rutenett til konvergensstudie. Små avvik ble registrert mellom rutenettene, mellom 2% og 6.2%. Stamp-momentet om

gravitasjonssenteret ble også målt og en gjennomsnittsverdi på $\overline{C_M} = -0.2563$ ble registrert (for det fineste rutenettet). Dette viste at den forenklede modellen var ustabil, som også er tilfellet i fullskala. Gjennom en mer detaljert studie av trykk- og hastighetsfordelinger i forskjellige plan ble problemområder identifisert. Usymmetri i trykkfordeling over og under ROV ble konkludert med å være hovedårsaken til ustabiliteten. En mulig løsning av problemet var å fjerne platen som er plassert akter i ROVen. Effekten av denne løsningen ble konkludert med å være tvilsom, ettersom det er plassert forskjellige komponenter foran platen som kan gi samme effekt på strømmen som platen. Omplassering av disse komponentene kan derfor være en nødvendighet.

Til slutt ble det konkludert med at det burde kjøres numeriske analyser uten platen, men med komponentene tilstede, for å undersøke påvirkningen fra disse. Numeriske simuleringer der disse komponentene er omplassert er også et interessant tilfelle å undersøke med tanke på stabiliteten til ROVen.

Contents

Project Description iii

Preface v

Summary vii

Sammendrag ix

Acronyms xvii

Nomenclature xxi

1 Introduction 1
- 1.1 Purpose of the Master's Thesis . . . 1
- 1.2 Remotely Operated Vehicle (ROV) . . . 1
  - 1.2.1 General . . . 1
  - 1.2.2 Merlin WR200 . . . 2
- 1.3 Simplifications of ROV for Flow Modelling Purposes . . . 4
  - 1.3.1 Rectangular Cubes . . . 4
  - 1.3.2 CAD Model . . . 5
- 1.4 Published work . . . 6
- 1.5 Definition of Terms . . . 7
- 1.6 Structure of the Master's Thesis . . . 7

2 Theoretical Background 9
- 2.1 Flow Around Bluff Bodies . . . 9
  - 2.1.1 Force Coefficients . . . 11
- 2.2 ROV Stability . . . 12
- 2.3 Computational Fluid Dynamics (CFD) . . . 12
  - 2.3.1 Courant Number . . . 14

2.3.2 Meshing 14
2.3.3 Mesh Quality 14
2.4 ANSYS FLUENT 15
2.4.1 ANSYS DesignModeler (DM) 15
2.4.2 ANSYS Meshing 15
2.5 Turbulence Modeling 16
2.5.1 General About Turbulence 16
2.5.2 Law of the Wall 16
2.5.3 Large Eddy Simulation (LES) 18
2.5.4 Detached Eddy Simulation (DES) 19
2.5.5 Unsteady Reynolds-Averaged Navier-Stokes (URANS) 19
2.5.6 The $k-\omega$ SST Turbulence Model 19

3 Stationary, Submerged Cube 21
3.1 Numerical Modeling of Fully Submerged Stationary Cube . . 21
3.1.1 Solver Setup 21
3.1.2 Computational Domain 22
3.1.3 Boundary and Initial Conditions 23
3.1.4 Mesh 24
3.1.5 Test Run 28
3.2 Simulation of Flow Around a Fully Submerged Stationary Cube 29
3.2.1 Grid Convergence Study 30
3.3 Discussion of Results 34
3.3.1 Drag Coefficient 34
3.3.2 Flow in the Wake of the Cubes 35
3.3.3 Vorticity 36
3.4 Conclusions 37

4 Merlin WR200 39
4.1 Modeling of Merlin WR200 ROV 39
4.1.1 Simplifying the CAD-model 39
4.1.2 Published Papers on the Topic 40
4.1.3 Solver Setup 42
4.1.4 Computational Domain and Boundaries 43
4.1.5 Mesh 45
4.2 Numerical Simulation of Flow Around Simplified Model of ROV 47
4.2.1 Grid Convergence Study 48
4.3 Discussion of Results 49
4.3.1 Force Coefficients 49

4.3.2 Velocities 52
4.3.3 Pressure Distribution 53
4.3.4 Effect of Plate 55
4.3.5 Vorticity 56
4.3.6 Comments Regarding the Stability of the ROV 59
4.4 Conclusions 60

5 Conclusions and Recommendations for Further Work 63
5.1 Conclusions 63
5.2 Recommendations for Further Work 64

References 67

A Mesh Quality I
A.1 Skewness I
A.2 Orthogonal Quality I
A.3 Aspect Ratio III
A.4 Smoothness III

B Details in the URANS Equations V

C Troubleshooting the Rounded Cube Case VII
C.1 Using the Realizable $k-\varepsilon$ Turbulence Model VII
C.2 Re = 5000 IX

D λ_2 Method XI

E Force Coefficients XIII
E.1 Sharp Edged Cube XIV
E.2 Round Edged Cube XV
E.3 ROV XVI

List of Tables

1.1 Main dimensions. 3

3.1 Test of sharp corners vs. rounded corners. 28
3.2 Grid convergence study for sharp edged cube. 30
3.3 Grid convergence study for round edged cube. 32

4.1 Grid convergence study for ROV. 48

D.1 Possible choices of eigenvalues [10]. XII

List of Figures

1.1 Merlin WR200 ROV. 3
1.2 Forward view from aft of ROV. 4
1.3 Cube shapes. 5
1.4 CAD model of Merlin WR200. 6
1.5 Naming of simplified ROV. 8

2.1 Flow over various rectangular cross sections [4]. 10
2.2 Separation of boundary layer for a circular cylinder [25]. . . . 10
2.3 The log-law [30]. 17

3.1 3D and 2D domain view. 23
3.2 Change in cell size due to surface proximity. 25
3.3 Mesh M1 and M3. 26
3.4 Cell-wall distance [m] for mesh M1. 27
3.5 Grid convergence for meshes M1 and M2. 31
3.6 Grid convergence for meshes M3 and M4. 33
3.7 Velocity profiles for sharp and rounded cube. 37
3.8 Vortical structures for meshes M1 and M3. 38

4.1 Modeled features of the ROV. 41
4.2 Frontview and backview of the simplified ROV. 43
4.3 Domain for ROV (identical for all meshes). 44
4.4 Mesh R2 for ROV (XY-plane). 46
4.5 Effect of rounded edges on back plate (mesh R2). 47
4.6 Regions where skewed cells may occur. 47
4.7 Grid convergence study for meshes R1, R2 and R3. 50
4.8 Fluctuation of the moment coefficient. 51
4.9 Iso-surfaces of u-velocity. 52
4.10 u- and v-component of the velocity in the XY-plane. 53
4.11 Streamlines through ROV. 54

4.12 C_p in the XY and XZ-plane. 54
4.13 Cp and ΔCp for ROV. 55
4.14 Components in front of the plate. 56
4.15 Instantaneous vortical structures for mesh R3. 58
4.16 Z-vorticity and turbulent intensity in the XY-plane. 61
4.17 Y-vorticity and turbulent intensity in the XZ-plane at $Y = -0.2\,\mathrm{m}$. 62

A.1 Cell skewness [3]. II
A.2 Vector definition. III
A.3 Distances for a unit cubical cell [3]. IV

C.1 Drag and lift coefficients for M3 and M4 using the $k-\omega$ SST model. VIII
C.2 λ_2 criterion at $t = 50\,\mathrm{s}$ for mesh M3. IX
C.3 Time series of drag coefficient using the realizable $k-\varepsilon$ model. IX
C.4 Iso-surfaces of λ_2 for mesh M3. X
C.5 C_D for M3 at $Re = 5000$. X

E.1 Drag and lift history and power spectral density for mesh M1 and M2. XIV
E.2 Drag and lift history and power spectral density for mesh M3 and M4. XV
E.3 Drag, lift and moment history for ROV (R1 and R2). XVI
E.4 Drag, lift and moment history for ROV (R3). XVII

Acronyms

2D	Two-Dimensional
3D	Three-Dimensional
CAD	Computer-Aided Design
CFD	Computational Fluid Dynamics
CFL	Courant-Friedrich-Lewy
COG	Center of Gravity
CURV	Cable-controlled Underwater Recovery Vehicle
DES	Detached Eddy Simulation
DM	DesignModeler
DNS	Direct Numerical Simulation
FFT	Fast Fourier Transform
FVM	Finite Volume Method
GRP	Glass-Reinforced Plastic
LES	Large Eddy Simulation
PDE	Partial Differential Equation
PISO	Pressure Implicit with Splitting of Operators
RANS	Reynolds-Averaged Navier-Stokes
ROV	Remotely Operated (underwater) Vehicle
SGS	Sub-Grid Scale
URANS	Unsteady Reynolds-Averaged Navier-Stoke

Nomenclature

α_1	Constant for the SST model
α_2	Constant for the SST model
β^*	Constant for the SST model
β_1	Constant for the SST model
β_2	Constant for the SST model
Δp	Pressure difference
Δt	Time step
Δx	Grid spacing in x-direction
δ	Boundary layer thickness
δ_{ij}	Kronecker delta
κ	Von Karman constant
λ_1	First eigenvalue of $\mathbf{S^2} + \mathbf{\Omega^2}$
λ_2	Second eigenvalue of $\mathbf{S^2} + \mathbf{\Omega^2}$
λ_3	Third eigenvalue of $\mathbf{S^2} + \mathbf{\Omega^2}$
$\mathbf{\Omega}$	Antisymmetric component of velocity gradient tensor
$\mathbf{J}$	Velocity gradient tensor
$\mathbf{S}$	Symmetric component of velocity gradient tensor
ν	Kinematic viscosity of the fluid
ν_t	Turbulent kinematic eddy viscosity
ω	Specific dissipation

Φ	Pitch angle
ρ	Density of the fluid
$\sigma_{\omega 1}$	Constant for the SST model
$\sigma_{\omega 2}$	Constant for the SST model
σ_{k1}	Constant for the SST model
σ_{k2}	Constant for the SST model
τ_w	Wall shear stress
θ	Roll angle
θ_e	Equiangular face/cell
$\theta_{\max}$	Max cell angle
$\theta_{\min}$	Min cell angle
$\vec{A_i}$	Area vector of face i
$\vec{c_i}$	Vector from cell centroid to neighbouring centroid for face i
$\vec{e_i}$	Vector from cell centroid to face center for face i
$\vec{f_i}$	Vector from cell centroid to face center for face i
A	Characteristic area for calculating force coefficients
a_1	Constant for the SST model
B	Width of ROV
BG_i	Distance between center of buoyancy and gravity in the ith direction
C	Constant in the log-law
c_1	Constant for the SST model
C_D	Drag coefficient
C_L	Lift coefficient
C_M	Moment coefficient
C_p	Pressure coefficient
C_μ	Constant for the SST model
CFL	Courant number

D	Characteristic length for calculating Reynolds number
D	Characteristic length for calculating Strouhal number
f_v	Vortex shedding frequency
g	Acceleration due to gravity
H	Height of ROV
I	Turbulent intensity
k	Turbulent kinetic energy
K_Φ	Restoring moment pitch
L	Length of ROV
l	Turbulent length
L_w	Recirculation length
M	Mass of ROV
M_θ	Restoringmoment roll
Re	Reynolds number
St	Strouhal number
U	Flow velocity in CFL-condition
u	Stream velocity
u^*	Shear velocity
u^+	Dimensionless velocity
U_∞	Free stream velocity
W	Gravity force
X	X-axis in co-ordinate system
Y	Y-axis in co-ordinate system
y	Distance from first node to the wall
y^+	Dimensionless distance from the first node to the wall
Z	Z-axis in co-ordinate system

Chapter 1

Introduction

1.1 Purpose of the Master's Thesis

The purpose of this Master's Thesis is to investigate numerically the flow behaviour around a Remotely Operated Vehicle (ROV). The ROV, named "Merlin WR200", is known to be subjected to an instability in survey mode (i.e. at constant speed) in both surge and sway. The instability is recognised by a pitching motion in surge and a rolling motion in sway. For this reason, it is wanted to investigate the flow around the ROV using Computational Fluid Dynamics (CFD) for identification of problem areas causing the instability. Suggestions for improvement is based on the identified problem areas.

Due to the high computational costs associated with CFD simulations in three dimensions, this thesis will only cover survey mode in surge.

1.2 Remotely Operated Vehicle (ROV)

1.2.1 General

A Remotely Operated Vehicle (ROV) is an unmanned underwater vehicle used in different subsea industries. Especially in the offshore hydrocarbon extraction industry, the ROV play an important role. The vehicle is controlled by an operator stationed on a surface vessel via an umbilical cable [32]. Most ROVs are built inside or around a rectangular frame with a flotation pack on top. The heavier equipment are placed as low as

possible to ensure that the center of gravity is lower than the center of buoyancy, and hence, that a sufficient stability is achieved. Strong hydraulic arms capable of carrying different tools for the specific task of the ROV are fitted in the front together with lights and cameras.

The first ROVs were developed in the 1950s for military purposes. In the 1960s, the US Navy developed ROVs for deep-sea rescue missions and for retrieving lost objects on the sea floor [32]. These vehicles were at that time called Cable-controlled Underwater Recovery Vehicle (CURV), and were the basis for the later development of the work class ROVs in the oil and gas industry [32].

In the oil and gas industry the ROV is used for a large variety of tasks, including inspections and maintenance of subsea structures, such as pipelines and manifolds, and aiding construction of subsea structures, such as connection of pipes and placing manifolds on the sea floor. The ROV also play an important role in science communities. They are used to study the deep oceans and its plants and animals. Many new species of plants and animals have been discovered by ROVs in depths otherwise impossible for divers to reach. A number of famous ship wrecks including the RMS Titanic and the German battleship Bismarck have been discovered using ROVs.

1.2.2 Merlin WR200

Figure 1.1 show the Merlin WR200 electrical work class ROV. It is designed to be the most efficient and reliable work class ROV on the market. The all electric propulsion system has the advantage of having all the control and power systems located topside. For this reason, reduced maintenance, increased reliability and power efficiency is achieved. An all electric propulsion system also has the advantage of minimizing leak of hydraulic fluid, which have been experienced with conventional ROVs.

Main Dimensions

The main dimensions of the Merlin WR200 ROV are as given in Table 1.1. The thickness of the top and bottom frame and side framework are not given. Using the CAD model provided by IKM Subsea these quantities can be measured. The top frame is found to have a thickness of 0.5 m and the bottom frame and sides are found to have a thickness of 0.2 m.

Figure 1.1: Merlin WR200 ROV.

Table 1.1: Main dimensions.

Dimension	Symbol	Value
Depth rating		3000 m
Length	L	2.8 m
Width	B	1.8 m
Height	H	1.7 m
Weight	M	2800 kg

General Data

The supporting frame of the ROV is made of an non-corrosive material and coated with Glass-Reinforced Plastic (GRP). GRP, or fiberglass, is a fiber reinforced polymer, where the plastic matrix is reinforced with fine fibers of glass [31]. The frame is filled with a buoyant material ensuring minimal volume and hence drag. The frame structure itself is open, ensuring easy access during inspection or maintenance of equipment (cf. Figure 1.2).

The Merlin WR200 have 8 electric driven thrusters, 4 for vertical thrust and 4 vectored for horizontal thrust. Figure 1.1 show how the horizontal thrusters are mounted in the top corners of the frame of the ROV.

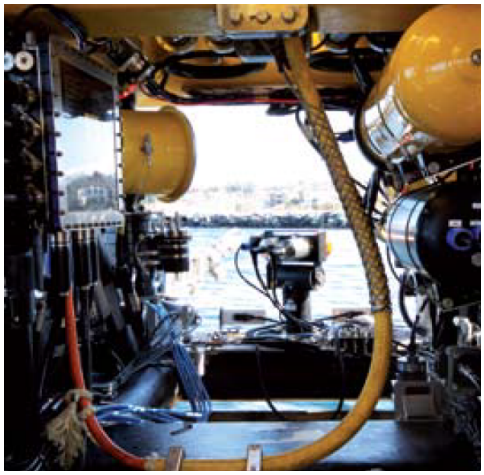

Figure 1.2: Forward view from aft of ROV.

1.3 Simplifications of ROV for Flow Modelling Purposes

Since the geometry of the Merlin WR200 is very complicated, this thesis will start by investigate the flow around two fully submerged stationary rectangular cubes; one with sharp edges and one with rounded edges. If the results for the two rectangular cubes are sound, the author feel confident that the same meshing technique and case setup should yield good results also for the simplified ROV model. Following is a description of the rectangular cube cases and the ROV model provided by IKM Subsea.

1.3.1 Rectangular Cubes

The rectangular cubes (from now on referred to as "cubes" in spite of their rectangular shape) are given dimensions that are consistent with the dimensions for the Merlin WR200 as given in Section 1.2.2. Figure 1.3 show the Merlin WR200 simplified as a cube both with sharp and rounded edges. To the authors' knowledge, there are no published results for flow around a fully submerged stationary cube to this date - which hence make validating the results more difficult. Ideally, both numerical simulation and experimental tests should have been performed, but this is not achievable due to limitations for the workload in the thesis.

(a) Sharp edges and corners. **(b)** Round edges and corners.

Figure 1.3: Cube shapes.

Figure 1.3a show the the cube with sharp edges and corners. The sharp edges may cause a high value of y^+ (which is the dimensional distance from the first node to the wall - which will be explained later) due to high induced shear velocities around the edges and corners. Hence, it is important to investigate the effect of rounding the edges of the cube (Figure 1.3b).

It is also important to study the behaviour of the drag for these two cases. The round corners and edges will certainly cause a lower drag than the sharp edges. Looking at the Merlin WR200 (e.g. Figure 1.4), it is seen that the framework consist mainly of rounded columns. Since it is expected that the rounded cube have less drag than the sharp, the rounded framework of the Merlin WR200 will have to be modeled on the simplified model.

1.3.2 CAD Model

After the simulations of the two cubes, a simplified model of the ROV will be made. A CAD (Computer-Aided Design) model of the Merlin WR200 have been provided by IKM Subsea (Figure 1.4). Using this model, the critical parts affecting the flow behaviour around and through the ROV may be identified. The model itself is however too complex to use for the CFD analysis and hence the simplified model will be made. In order to be representative, this simplified model will have to be able to capture the main flow behaviour as for the real case. The making of this model is further discussed in Section 4.1.1.

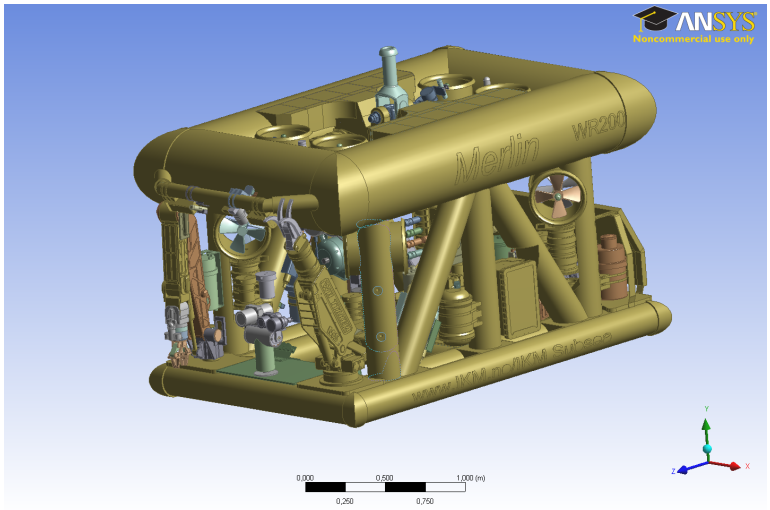

Figure 1.4: CAD model of Merlin WR200.

1.4 Published work

As briefly mentioned, there have not (at least to the authors' notice) been performed any numerical studies of the flow around a fully submerged stationary cube. White [29] reports a drag coefficient of $C_D = 1.07$ for $Re \geq 1 \times 10^4$ based on frontal area of the cube - he does however not state if this value is numeric, experimental or theoretic. There have however been made many studies of the flow around surface mounted cubes at moderate to high Reynolds numbers. These are among others Gao and Chow [7], Lakehal and Rodi [12], Paterson and Apelt [18], Rodi [20] and Yakhot, Liu, and Nikitin [35]. These authors have mainly studied the distribution of the turbulent kinetic energy, k, for different turbulence models and the separation and reattachment of vortices on top and behind the cube.

Lee [13] reported a mean drag coefficient (C_D) of 2.04 and a Strouhal number (St) of 0.122 for a two-dimensional (2D) square cylinder at $Re = 1.76 \times 10^5$. This was achieved by a wind tunnel experiment, using pressure tappings for measuring the pressure. The force coefficients were obtained by integrating the mean pressure distribution (C_p). Schewe [21] investigated among other an inclined square cylinder, reporting $C_D = 2.4$ and $St = 0.12$ at $Re = 6 \times 10^5$ (found in Ahlborn, Seto, and Noack [1]).

The most interesting work is probably the "Applied Fluid Dynamics Handbook" by Blevins [4]. This work includes a thorough review of published results for the drag coefficient (and other hydrodynamic quantities such as Strouhal number) for different shapes of bluff bodies. The results are presented in tables as function of key geometric relations (e.g. L/D). This work will thus be essential for validating the results for the two cubes.

Tian et al. [27] investigated the flow normal to a flat plate at $Re = 1.5 \times 10^5$ in both 2D and 3D. In the 2D case, the URANS equations were used in conjunction with the $k-\omega$ SST turbulence model. The 3D simulations were carried out using LES and the Sub-Grid Scale (SGS) model by Smagorinsky [23]. The aim was to investigate the 3D effects of the flow normal to a flat plate. The results showed that the 2D simulations were not able to capture these 3D effects. The 3D simulations were in good agreement with experimental results. Tian et al. [27] and Blevins [4] will be further discussed later in this thesis.

There are few published papers of CFD simulations of ROVs. Some publications have used CFD of entire ROV structures for estimation of drag force and pressure center for design purposes (e.g. [6, 8, 19]), while others have focused on the thruster units and prediction of thrust and torques (e.g. [16, 28]). These will be further discussed in Section 4.1.2.

1.5 Definition of Terms

In this Master's Thesis, different terms are used. For the discretised domain, both "grid" and "mesh" are used and have the same meaning. "Eddy" is also used and have the same meaning as "vortex". When describing the simplified ROV, the terms "sides", "plate", "top frame" and "bottom frame" are used. These are shown in Figure 1.5. The last remark is regarding the dimensionless distance from the surface to the first node, y^+. This is for *all* directions (not just y-direction).

1.6 Structure of the Master's Thesis

This section give a short description on the following chapters in this Master's Thesis.

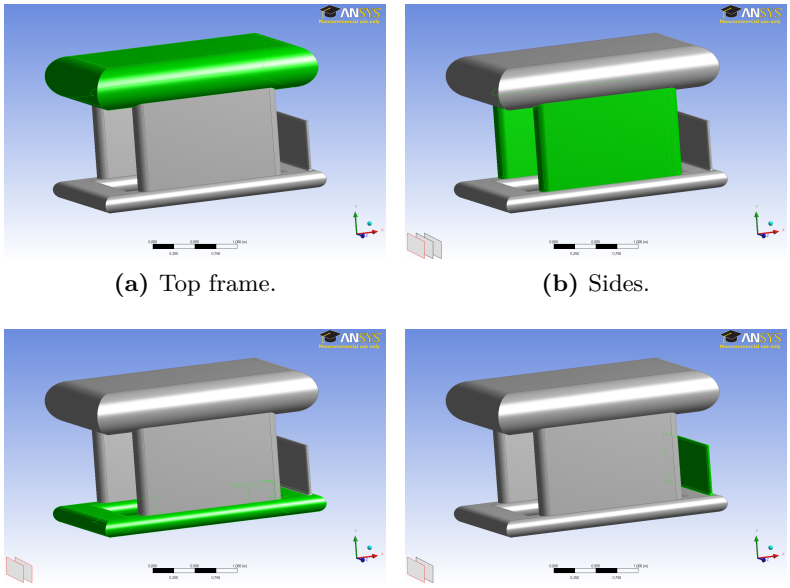

(a) Top frame. **(b)** Sides.

(c) Bottom frame. **(d)** Plate.

Figure 1.5: Naming of simplified ROV.

Chapter 2 is a theoretical chapter. Here, the basics for flow around bluff bodies, general ROV stability (as given by [8]), basics for CFD, CFD software to be used, meshing and turbulence modeling will be described.

Chapter 3 addresses the case with the two cubes. First, the general case setup is described (computational domain, boundaries, reference values etc.). Then there is a short description of the test runs to be performed. The test runs are performed in order to assure that the simulations do not crash and for adjusting the distance from the first node to the surface. Next, the results from the grid convergence study are presented together with a more thorough discussion of the results.

Chapter 4 addresses the case with the Merlin WR200 ROV. This chapter begin with an investigation of the CAD model and the making of the simplified model for the simulation. Following is a discussion of the quality of the mesh. The results of the grid convergence study are then presented together with a discussion of the results with regards to the instability problem. Problem areas are identified by examining the results.

Chapter 5 give the final conclusions and recommendations for further work to be done on the same topic.

Chapter 2

Theoretical Background

2.1 Flow Around Bluff Bodies

The flow around a two-dimensional circular cylinder have been studied by numerous authors (both numerically and experimentally), and the theory of the flow behaviour is well documented in different literature (e.g. by Sumer and Fredsoe [25], White [29] and Zdravkovich [36]). However, for the flow around square cylinders and cubes, there exist almost no literature of the theory. The "Applied Fluid Dynamics Handbook" by Blevins [4] does discuss among other drag coefficient for non-circular cross-sections and other bluff bodies. Figure 2.1 is taken from this book and show drag coefficient for various rectangular cross sections. Some publications also have, to some extent, discussed briefly the basic theory for flow around square cylinders.

The main difference for the flow behaviour around a circular and around a square cylinder, is that for the square cylinder the separation points are fixed to the upstream corners. For this reason, the effect of increasing Reynolds number is not as important for square cylinders as for circular cylinders. For the case of a circular cylinder, the separation points change with Reynolds number and hence the forces acting on the cylinder also varies.

In order to understand why vortices are created, one need to understand the physics of the flow behaviour on the surface of a body in a viscous flow. The no-slip condition state that the velocity have to be zero (or equal if the cylinder is not stationary) on the cylinder surface and hence a boundary layer (with thickness δ) is formed. When separated, the free shear layer tend to curl inward, creating a vortex. This is due to the velocity gradient

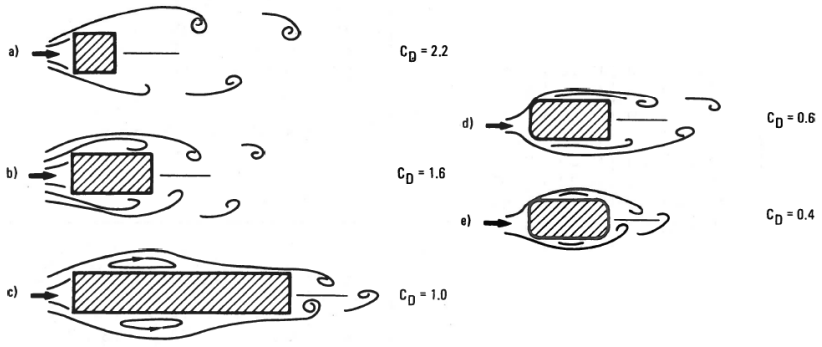

Figure 2.1: Flow over various rectangular cross sections [4].

as shown in Figure 2.2 for the case of a circular cylinder. The vortices are then shed in an alternate process.

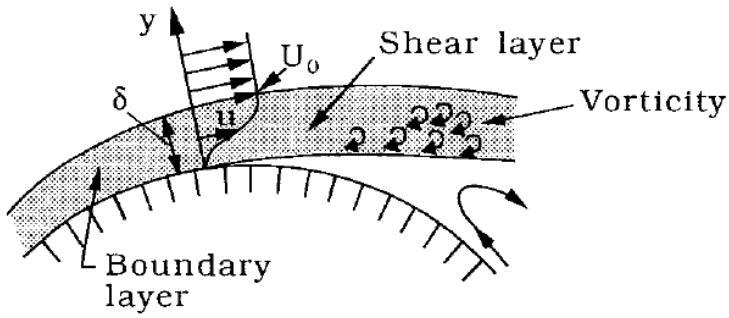

Figure 2.2: Separation of boundary layer for a circular cylinder [25].

The alternate vortex shedding is a result of one vortex cutting off the supply of vorticity to the other one, which then is shed. A new vortex is then formed and starts to grow and eventually cuts off the supply of vorticity to the first vortex. This vortex shedding results in forces acting on the cylinder. The drag force arises from the fact that the fluid is viscous and varies with the width of the wake. In an inviscid flow, the drag force would be zero due to flow symmetry. This phenomenon is called D'Alemberts Paradox and arises from the fact that there is no separation. The lift force is due to the alternate vortex shedding and hence the instantaneous lift force changes sign for each vortex shedding, resulting in a zero mean force. Only when the separation is partly laminar and partly turbulent can the mean lift force

be non-zero.

2.1.1 Force Coefficients

The dimensionless force and pressure coefficients are given as:

$$C_D = \frac{Drag}{\frac{1}{2}\rho U_\infty^2 A} \tag{2.1}$$

$$C_L = \frac{Lift}{\frac{1}{2}\rho U_\infty^2 A} \tag{2.2}$$

$$C_M = \frac{Moment}{\frac{1}{2}\rho U_\infty^2 AL} \tag{2.3}$$

$$C_p = \frac{\Delta p}{\frac{1}{2}\rho U_\infty^2} \tag{2.4}$$

Here ρ is the density of the fluid, A the characteristic area (e.g. frontal area of cube or span-wise length of square cylinder) and L characteristic length. Furthermore, the Strouhal number, which is the dimensionless vortex shedding frequency (f_v), is defined as:

$$St = \frac{f_v D}{U_\infty} \tag{2.5}$$

Here, D is the diameter of a circular cylinder or span-wise length of a square cylinder. For the cube and ROV, the height is used as characteristic length. The Strouhal number is dependent on the Reynolds number, which defines the vortex shedding process. However, since the separation points for square and rectangular cylinders are for most cases fixed to the leading corners, the flow will not vary as much as for the case of a circular cylinder. The Reynolds number is calculated using the flow velocity (U_∞), kinematic viscosity (ν) and characteristic length (D) as:

$$Re = \frac{U_\infty D}{\nu} \tag{2.6}$$

2.2 ROV Stability

A general stability analysis and a theoretical investigation of the drag force acting on the ROV can be of importance, both for validating CFD results and evaluating the thruster locations. Gomes et al. [8] did such an analysis for a similar ROV. The ROV they investigated had the same arrangement of vectored thrusters in the four frame corners of the vehicle as the Merlin WR200.

In their paper, they set up a set of equations for the restoring moments on pitch and roll:

$$K_\Phi = -BG_y W\cos(\theta)\cos(\Phi) + BG_z W\cos(\theta)\sin(\Phi) \tag{2.7}$$

$$M_\theta = BG_z W\sin(\theta) + BG_x W\cos(\theta)\cos(\Phi) \tag{2.8}$$

Here, W is the gravity force ($W = Mg$, where $g = 9.81\,\mathrm{m/s^2}$) and BG_i is the distance between the center of gravity and the center of buoyancy in the three directions ($1-3$ or X, Y and Z). These equations can then be used to set demands for passive roll and pitch stability. The restoring forces should be zero for zero angles, both in pitch and roll. If these angles are non-zero, the restoring forces should bring the angles back to zero. According to [8], the first condition demand that both BG_x and BG_y are zero - i.e. the center of buoyancy and the center of gravity are on the same coordinate in the XY-plane. The second condition then require BG_z (i.e. the metacentric height) to be different from zero. Now Equation (2.7) and (2.8) can be written as:

$$K_\Phi = BG_z W\cos(\theta)\sin(\Phi) \tag{2.9}$$

$$M_\theta = BG_z W\sin(\theta) \tag{2.10}$$

The last two equation show that the pitch and roll moment are proportional to the metasentric height for given pitch and roll angles.

Further, the authors states the importance of the thruster force being aligned with the drag force. If this is achieved, the ROV will not suffer any moment in pitch or roll for pure longitudinal or lateral motion. Hence, the vertical placement of the Merlin WR200s thrusters may be an issue to address when the pressure distribution on the ROV itself is revealed.

2.3 Computational Fluid Dynamics (CFD)

Computational Fluid Dynamics (CFD) is a way of analysing fluid flows numerically on a computer by a set of algebraic equations. The algebraic

equations are obtained by discretising the partial differential equations (PDEs), which may be conservation of mass, momentum, energy etc. The solution is attained at discrete points and hence the computational domain need to be discretised into discrete areas or volumes - which is the mesh or grid. For this reason, the grid resolution is of great importance. For instance, in order to fully describe the physics of the flow close to a wall, the grid resolution need to be very fine. Generally, areas with abrupt changes in geometry or adverse pressure gradients need to have a fine grid resolution. However, it is also important to be able to identify areas where the grid can be more coarse. Hence, a good grid could spare the user for an unnecessarily high cell count and thus also computational demands.

CFD also allow the user to study fluid phenomena at very small scales, which otherwise would be impossible in an experimental test. By studying the phenomena in slow motion, a greater understanding of the physics may be achieved. Economically, numerical simulations are much cheaper than experimental tests.

When performing numerical analysis, it is important to ensure that the numerical errors are as small as possible. Except from the error associated with the fact that the solution is attained at discrete points in the domain, there are three important sources of error; Firstly, the governing equations need to be able to describe the fluid flow in a satisfactory way. This lead to the second source of error which is the algebraic equations and lastly the physical models used in the simulation (e.g. turbulence models).

The general procedure when performing CFD analysis, is:

1. Identify problem (define goals and domain).

2. Pre-processing (geometry, mesh, physics and solver settings).

3. Solve.

4. Post-processing (examine and evaluate/validate results).

If the results (step 4) are not satisfactory, one need to either change geometry, mesh or solver settings. This loop continues until the results are satisfactory.

2.3.1 Courant Number

An important condition for convergence when performing CFD analysis, is the Courant-Friedrich-Lewy (CFL) condition, or simply the Courant number. For a given flow velocity U, time step Δt and cell size Δx it is:

$$CFL = U\frac{\Delta t}{\Delta x} < 1 \tag{2.11}$$

The most simple way of explaining this condition is that the fluid particles should not travel more than the grid spacing for each time step. If $CFL \gg 1$, it would mean that the fluid particles were travelling more than the grid spacing for each time step, and hence the mesh would not be able to describe the physics of the flow.

2.3.2 Meshing

The mesh, or grid, is the discretised domain in which the flow problem is to be solved. The flow properties are calculated in each cell, and hence, as briefly described, the density of the cells (i.e. the mesh resolution) is of great importance. Basically, the grid could be either structured or unstructured. In an unstructured grid, the cells are arranged in an apparently random fashion in contrast to a structured grid. Further, the mesh could be either single-block or multi-block. For instance, in a structured single-block mesh, the grid lines must pass through the entire domain. For complex geometries, multi-block grids is a necessity.

2.3.3 Mesh Quality

The quality of the mesh is measured using three factors; skewness, smoothness and aspect ratio (more about mesh quality in Appendix A). Also, different cell types may be preferred over others, typically hexahedral meshes with the grid lines aligned with the flow are preferred over tetrahedral meshes if the cell count is the same. Generally, hexahedral meshes give a lower cell count than tetrahedral and are regarded as numerically more stable.

2.4 ANSYS FLUENT

For this Master's Thesis, the CFD-package FLUENT from ANSYS Inc. is used. ANSYS FLUENT is able to perform incompressible and compressible modeling of both laminar and turbulent fluid flows. The user can choose to use either a steady-state or a transient solver. The ANSYS CFD-solvers are based on the Finite Volume Method (FVM). The control volumes in FLUENT are cell-centered, meaning that they correspond directly with the mesh. The computational domain is discretised into a finite set of control volumes where the conservation equations (as given by [2]) are solved:

$$\underbrace{\frac{\partial}{\partial t}\int_V \rho\phi dV}_{\text{Unsteady}} + \underbrace{\oint_A \rho\phi V \cdot dA}_{\text{Convection}} = \underbrace{\oint_A \Gamma_\phi \nabla\phi \cdot dA}_{\text{Diffusion}} + \underbrace{\int_V S_\phi dV}_{\text{Generation}} \tag{2.12}$$

Here, ρ is the density of the fluid, V volume, A area and ϕ a conserved quantity (e.g. energy, momentum etc.). The partial differential equations are then discretised into a set of algebraic equations, which are solved numerically, on the form:

$$\mathbf{Au} = \mathbf{b} \tag{2.13}$$

Where $\mathbf{A}$ is an $n \times n$ matrix of known quantities, $\mathbf{u}$ a column vector containing the unknowns and $\mathbf{b}$ a column vector of known quantities.

2.4.1 ANSYS DesignModeler (DM)

The geometry and computational domain is created using ANSYS DesignModeler (DM). This is an application accessed from the ANSYS Workbench. DM give the user two options, either to import a model from CAD (Computer-Aided Design model) or to create a specific geometry from scratch.

2.4.2 ANSYS Meshing

When the geometry and the domain have been created, one proceeds to ANSYS Meshing to generate the mesh of the domain (see Section 3.1.4 for further details). Here, details of the mesh (e.g. mesh quality as presented in Appendix A) may be studied after the mesh have been generated.

2.5 Turbulence Modeling

2.5.1 General About Turbulence

Turbulence is a three-dimensional (3D) phenomenon. It is characterized by an apparently random and chaotic fluid motion, or, vorticity. Hinze [9] give the following definition of turbulence:

"*Turbulent fluid motion is an irregular condition of flow in which the various quantities show a random variance with time and space coordinates, so that statistically distinct average values can be discerned*"

If a flow is turbulent, the turbulence will dominate over the other fluid phenomena and cause increased mixing, energy dissipation, drag and heat transfer [5]. The flows of engineering interest, can for most cases be considered as turbulent due to the fact that the fluid is viscous and that the scales and velocities are large (e.g. flow past rockets, airplanes, ships etc. as stated by Wilcox [34]). Only for small scales and low velocities can the effect of turbulence be disregarded as the flow is laminar.

2.5.2 Law of the Wall

The law of the wall is an empirically-determined relationship for turbulent flows in close proximity to a wall (or other solid boundaries). It states that the streamwise velocity in the flow near the wall varies logarithmically with the distance to the wall [34]. It is also known as the logarithmic law of the wall - or simply the log-law. It can be written as given by White [29]:

$$\frac{u}{u^*} \approx \frac{1}{\kappa} \ln\left(\frac{yu^*}{\nu}\right) + C \tag{2.14}$$

Here u is the stream velocity, u^* the shear velocity, y distance to the wall, ν the kinematic viscosity of the fluid, κ the Von Karman constant and C a constant. Equation (2.14) can be made dimensionless as:

$$u^+ = \frac{1}{\kappa} \ln\left(y^+\right) + C \tag{2.15}$$

Where $u^+ = u/u^*$ and $y^+ = yu^*/\nu$ is dimensionless velocity and distance to the wall, respectively. For smooth surfaces $C = 5.0$, while $\kappa = 0.41$ holds for both smooth and rough surfaces [34]. The wall shear stress can then be found as:

$$\tau_w = \rho(u^*)^2 \tag{2.16}$$

The log-law is however only valid in the log-law region, which typically is $30 \leq y^+ \leq 200$ as seen in Figure 2.3. Further, it is seen that in the

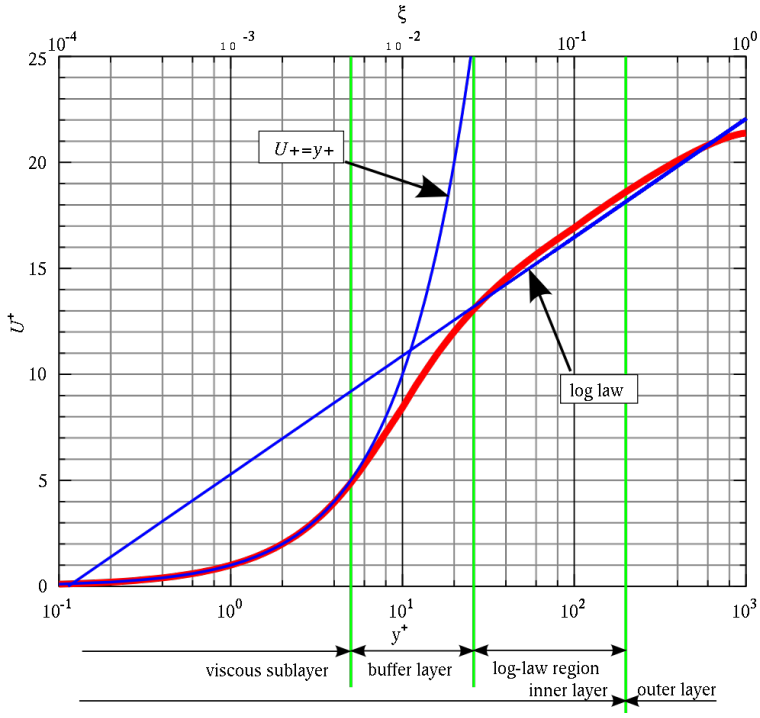

Figure 2.3: The log-law [30].

viscous sublayer (i.e. $y^+ \leq 5$), the linear approximation ($u^+ = y^+$) holds, while neither the linear nor the log-law holds in the buffer layer ($5 \leq y^+ \leq 30$). This is handled by using the linear approximation close to the viscous sublayer and the log-law close to the log-law region (switching at $y^+ = 11$ [30]).

In the log-law region, i.e. $30 \leq y^+ \leq 200$, wall functions are used for modeling the velocity profile and calculating the properties of the flow. The wall function assumes that the flow close to the wall behaves like a fully developed turbulent flow.

2.5.3 Large Eddy Simulation (LES)

This mathematical model for turbulence was proposed in 1963 by Joseph Smagorinsky. As the name "Large Eddy Simulation" suggests, the LES approach only resolve the larger eddies. This is done using a low-pass filtering of the Navier-Stokes equations and hence eliminating the small scales of the solution, reducing the computational cost for the simulation. Compared with Direct Numerical Simulation (DNS) and Reynolds-Averaged Navier-Stoke (RANS), LES lies in between in terms of computational demands. Using LES, the grid of the computational domain can be more coarse and the time step larger compared with DNS since the small scale motions are modeled using a sub-grid scale (SGS) model. This means that the eddies which are smaller than the cell size are removed and modeled by the SGS model, hence the grid itself is the filter.

Ansys Fluent have the following SGS models available [2]: Smagorinsky-Lilly, WALE (Wall-Adapting Local Eddy-Viscosity), Dynamic Smagorinsky-Lilly and Dynamic Kinetic Energy Transport.

For a given scalar ϕ, the following holds:

$$\phi_i = \overline{\phi_i} + \phi_i' \tag{2.17}$$

Here, the last term is the fluctuating (SGS) part and $\overline{\phi_i}$ the resolvable scale part. The incompressible Navier-Stokes equation of motion is:

$$\frac{\partial u_i}{\partial t} + u_j \frac{\partial u_i}{\partial x_j} = -\frac{1}{\rho}\frac{\partial p}{\partial x_i} + \frac{\partial}{\partial x_j}\left(\nu \frac{\partial u_i}{\partial x_j}\right) \tag{2.18}$$

Now, inserting for $u_i = \overline{u_i} + u_i'$ and $p = \overline{p} + p'$ and filtering the equation, the equation of motion for the resolved field is:

$$\frac{\partial \overline{u_i}}{\partial t} + \overline{u_j}\frac{\partial \overline{u_i}}{\partial x_j} = -\frac{1}{\rho}\frac{\partial \overline{p}}{\partial x_i} + \frac{\partial}{\partial x_j}\left(\nu \frac{\partial \overline{u_i}}{\partial x_j}\right) + \frac{\partial \tau_{ij}}{\partial x_j} \tag{2.19}$$

Here, τ_{ij} is the SGS turbulent stress given as:

$$\tau_{ij} = \rho(\bar{u_i}\bar{u_j} - \overline{u_i u_j}) \tag{2.20}$$

Here, $i, j = 1 - 3$. x_1, x_2 and x_3 then denote the streamwise, vertical and cross-flow directions and u_1, u_2 and u_3 the corresponding velocities (also referred to as u, v and w), respectively. ν is the kinematic viscosity and p the instantaneous dynamic pressure. Primed quantities are the fluctuating part of the instantaneous value - which are filtered.

2.5.4 Detached Eddy Simulation (DES)

Standard LES models may have difficulties in areas in close proximity to a wall. Since LES does not use wall functions, there is a high resolution requirement for the grid in the boundary layer, typically $y^+ \sim 1$. In addition, a LES simulation need to be run for a sufficiently long flow-time in order to obtain stable statistics of the flow. This result in higher computational demands when running LES simulations compared with stable RANS simulations.

In order to achieve both the advantage of a coarser mesh in the outer region (achieved by LES) and to avoid the need for a high grid resolution in the boundary layer (RANS models), hybrid models combining the unsteady RANS models in the boundary layer and LES treatment in the separated regions have been developed. Detached Eddy Simulation (DES) by Spalart et al. [24] is such a hybrid model. In the current work, LES in conjunction with the unsteady RANS equations and the $k-\omega$ SST turbulence model is used.

2.5.5 Unsteady Reynolds-Averaged Navier-Stokes (URANS)

In the near-wall regions of the cubes and ROV, the Unsteady Reynolds-Averaged Navier-Stokes (URANS) equations are used. The Reynolds-averaged equations for conservation of mass and momentum for an unsteady, incompressible, viscous and turbulent flow are:

$$\frac{\partial \overline{u_i}}{\partial x_i} = 0 \tag{2.21}$$

$$\frac{\partial \overline{u_i}}{\partial t} + \overline{u_j}\frac{\partial \overline{u_i}}{\partial x_j} = -\frac{1}{\rho}\frac{\partial \overline{p}}{\partial x_i} + \nu\frac{\partial^2 \overline{u_i}}{\partial x_i^2} - \frac{\partial \overline{u_i' u_j'}}{\partial x_j} \tag{2.22}$$

Here, i, j are as described for the LES equations. The last term in Equation (2.22) is the Reynolds stress component, $\overline{u_i' u_j'}$ (see Appendix B for details regarding further relations and constants).

2.5.6 The $k-\omega$ SST Turbulence Model

In the areas close to the surface of the ROV, the URANS equations will be used in conjunction with the $k-\omega$ SST (Shear Stress Transport) model

of Menter [14]. This model is basically a combination of the $k-\omega$ model by Wilcox [33] and the standard $k-\varepsilon$ model by Jones and Launder [11]. Close to the cylinder surface, i.e. in the near-wall region, the original $k-\omega$ model is used. In the free shear layers and in the outer wake region, the standart $k-\varepsilon$ model is used. Compared with other two-equation models, the $k-\omega$ SST model have shown to be specially good in adverse pressure gradient areas and separating flows. The equations for k and ω are given from Menter, Kuntz, and Langtry [15] as:

$$\frac{D(\rho k)}{Dt} = \tilde{P}_k - \beta^* \rho \omega k + \frac{\partial}{\partial x_j}\left[(\mu + \sigma_k \mu_t)\frac{\partial k}{\partial x_j}\right] \tag{2.23}$$

$$\frac{D(\rho \omega)}{Dt} = \alpha \rho S^2 - \beta^* \rho \omega^2 + \frac{\partial}{\partial x_j}\left[(\mu + \sigma_\omega \mu_t)\frac{\partial \omega}{\partial x_j}\right] + 2(1-F_1)\rho \sigma_{\omega 2}\frac{1}{\omega}\frac{\partial k}{\partial x_j}\frac{\partial \omega}{\partial x_j} \tag{2.24}$$

Where $\tilde{P}_k$ is a production limiter for avoiding build-up of turbulence in stagnation regions and F_1 a blending function. These are given as:

$$\tilde{P}_k = min\left[\mu_t \frac{\partial u_i}{\partial x_j}\left(\frac{\partial u_i}{\partial x_j} + \frac{\partial u_j}{\partial x_i}\right), 10\beta^* \rho k \omega\right] \tag{2.25}$$

$$F_1 = \tanh\left(\left[min\left\{max\left(\frac{\sqrt{k}}{\beta^* \omega y}, \frac{500\nu}{y^2 \omega}\right), \frac{4\rho \sigma_{\omega 2} k}{CD_{k\omega} y^2}\right\}\right]^4\right) \tag{2.26}$$

Here y is the distance to the nearest wall. In the near-wall region, $F_1 = 1$, while it goes to zero in the outer region. $CD_{k\omega}$ is given as:

$$CD_{k\omega} = max\left(2\rho \sigma_{\omega 2}\frac{1}{\omega}\frac{\partial k}{\partial x_j}\frac{\partial \omega}{\partial x_j}, 10^{-10}\right) \tag{2.27}$$

The standard $k-\varepsilon$ model has two weaknesses; it overpredicts the shear stress in adverse pressure flows and requires a modification for near-wall cases. The latter weakness is solved in the $k-\omega$ SST model by a limitation of the shear stress. For further details of the constants and relations used in this model, see Appendix B.

Chapter 3

Stationary, Submerged Cube

3.1 Numerical Modeling of Fully Submerged Stationary Cube

In order to have a set of reference values for the hydrodynamic quantities to be calculated for the ROV, numerical simulation of the flow around a fully submerged stationary cube is performed. Due to flow symmetry in both XY-plane and XZ-plane, the mean lift and hence also moment coefficients should be zero. The simulation is performed at $Re = 8.5 \times 10^5$, which corresponds to a velocity of one knot in seawater conditions (i.e. $\rho = 1025\,\mathrm{kg/m^3}$, $\nu = 1 \times 10^{-6}\,\mathrm{m^2/s}$ and $U_\infty = 0.5\,\mathrm{m/s}$).

3.1.1 Solver Setup

The solver used in this present study is the transient pressure-based solver. This solver takes pressure and momentum as primary variables. Further, the flow model used is the Detached Eddy Simulation (DES), which is a hybrid model consisting of LES in the outer region and URANS in conjunction with the $k - \omega$ SST turbulence model in the near-wall region.

The calculations are carried out using the PISO (Pressure Implicit with Splitting of Operators) scheme. Further, the spatial schemes used are "Green-Gauss Cell Based", "PRESTO!", "Bounded Central Differencing", "Second Order Upwind", "Second Order Upwind" and "Second Order Implicit" for gradient, pressure, momentum, turbulent kinetic energy,

specific dissipation rate and transient formulation, respectively.

The force coefficients, as described in Chapter 2, are calculated on the following reference values:

$$\begin{aligned} A &= 3.06\,\mathrm{m}^2 \\ L &= H = 1.7\,\mathrm{m} \\ p &= 0\,\mathrm{Pa} \\ \rho &= 1025\,\mathrm{kg/m}^3 \\ \nu &= 1 \times 10^{-6}\,\mathrm{m}^2/\mathrm{s} \end{aligned} \tag{3.1}$$

Here, A is the projected frontal area of the cube and ρ the density of seawater.

The numerical simulations are run on "Njord", a supercomputer located at NTNU in Trondheim. "Njord" have an IBM p575+ system with 192 nodes and a total of 2976 cores (each 1.9 GHz). The cases are run in batch mode, which mean that the simulations are controlled by a "job" and a "journal" file. These scripts then read the case and data files created by FLUENT. Output is produced as specified by the user and also written into separate case and data files for further post-processing.

3.1.2 Computational Domain

The computational domain is of great importance when performing CFD simulations. If the computational domain is too small, far field effects from the surrounding boundaries may cause non-realistic or polluted results. For instance, if symmetry boundaries are used, which mean that the flow can only travel parallel to the boundary, a too small computational domain would clearly disrupt the flow around the given body.

In order to ensure that there is no effect from the surrounding boundaries, the inlet, top, bottom and sides of the domain is at a distance of $7B$ from the origin (B being the width of the ROV). The outlet is then placed $21B$ downstream of the origin. Hence, the total size of the domain is $14B \times 14B \times 28B$ (Figure 3.1a). The origin is placed in the center of the cube, with X positive downstream, Y positive upwards and Z positive to the port side of the cube and ROV.

In order to control the mesh around the cube, two smaller domains have been created. The inner domain is made close to the cube in order to get

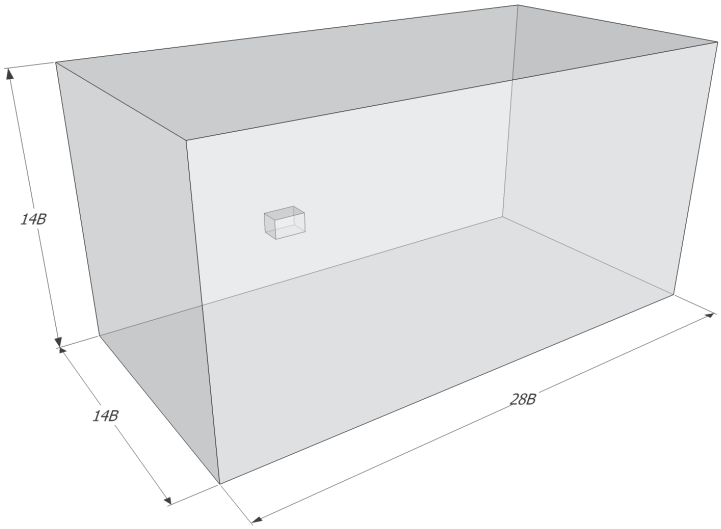

(a) 3D view of the domain. Inlet to the left, outlet to the right.

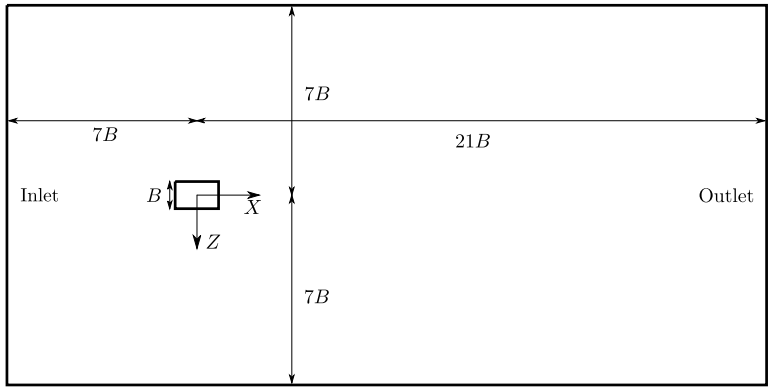

(b) 2D view of the domain (XZ-plane).

Figure 3.1: 3D and 2D domain view.

the desired resolution of the boundary layer. The middle domain stretches $3H$ into the wake (H being the height of the ROV - and hence also the cube) to capture the behaviour of the vortices.

3.1.3 Boundary and Initial Conditions

When performing CFD analysis, two type of boundary conditions (BC) applies. These are Neumann and Dirichlet types. Dirichlet type BC

describes the value of a variable, while the Neumann type BC describes the gradient of a variable normal to the boundary.

The domain is divided into the following boundaries:

- Inlet
- Outlet
- Cube
- TopBottomSides

The inlet is defined as "velocity-inlet". Here the inflow velocity (i.e. U_∞) is defined according to the desired value of one knot (Dirichlet type). Further, the turbulent length is set as $l = 0.0045H = 0.007\,65\,\text{m}$ and the turbulent intensity $I = 0.8\%$.

The outlet is defined as "pressure-outlet". Here the gauge pressure is set equal to zero and l and I are as for the inlet.

The cube surface is defined as a "wall". This means that the no-slip condition is taken into account on the entire surface of the cube. Hence, the velocity have to be zero on the surface. The normal velocity on the surface is also equal to zero, hence there can be no flow through the surface of the cube/ROV.

The last boundary is the top, bottom and sides of the computational domain. These have been given "symmetry" boundary conditions. This mean that the normal velocity and normal gradients (Dirichlet and Neumann type) of all variables are zero.

3.1.4 Mesh

CutCell Meshing

The meshes of the domain have been made using the "CutCell" method. This is an cartesian patch independent meshing method designed for Ansys Fluent.

The general process of the CutCell meshing start with the user specifying the size functions, for instance minimum cell size and growth rate. The maximum cell size is then calculated according to the input. Then the initial size of the Cartesian grid is computed based on the values set in the

size function. At first, a uniform grid is created within the entire domain. Then, using the size function, the grid is refined according to specifications made by the user. The next step is projecting the nodes in the cells which intersect with the geometry, to the geometry. The mesh outside of any body (the body being the fluid for this case) is then removed and the boundary mesh is recovered and separated based on the underlying geometry.

The CutCell process creates hanging nodes (red circles in Figure 3.2) where the cell size change (e.g. close to a surface). This is however not a problem for Ansys Fluent. Two faces then share the same plane where a hanging node occurs (Fluent treats hanging nodes in the same way as polyhedral meshes).

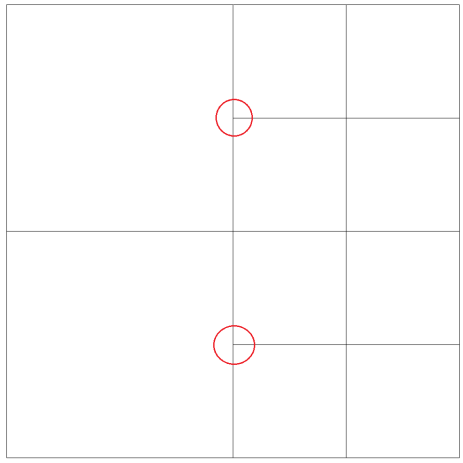

Figure 3.2: Change in cell size due to surface proximity. Outer domain to the left.

Details of Generated Mesh

In order to get the desired grid resolution in the boundary layer, an inflation layer have been created on the cube surface. This consist of 10 layers which grow by 10% for each grid point. The distance from the wall to the first grid point is controlled and can thus be varied in order to get the desired value of y^+. Outside the layer, the domain is meshed using the CutCell method, with a 10% increase in cell size until the maximum cell size is 0.64 m (8% increase for refined mesh (M2 and M4 cf. Table 3.1 on page 28)).

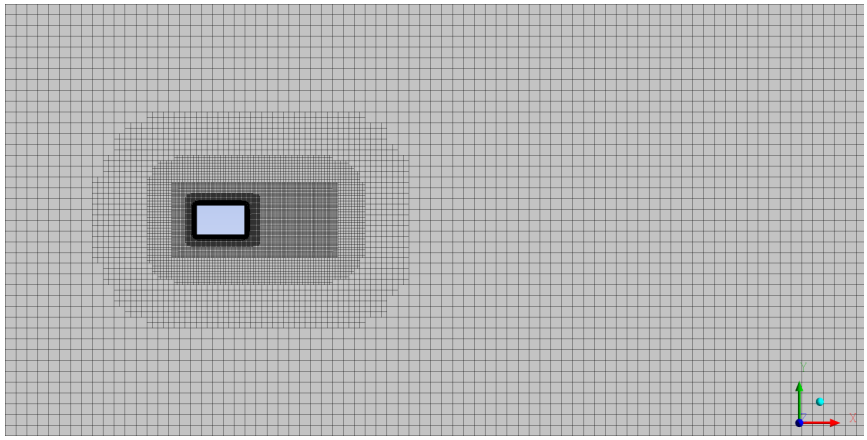

(a) Entire domain (XY-plane).

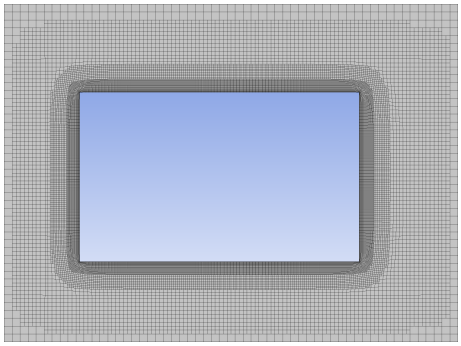

(b) Close-up on cube (M1).

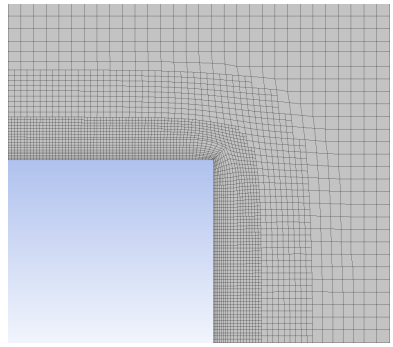

(c) Close-up on corner (M1).

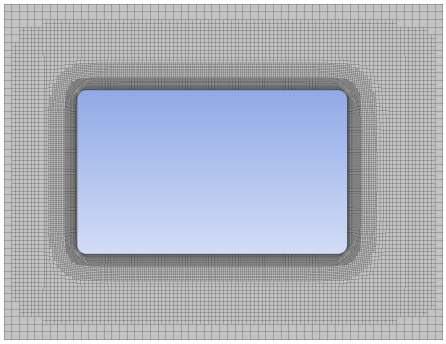

(d) Close-up on cube (M3).

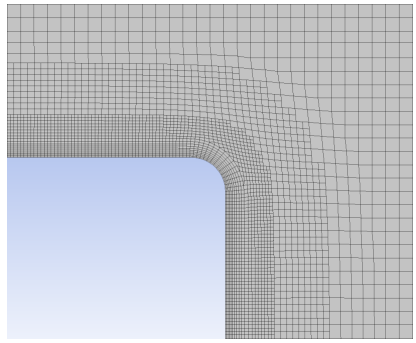

(e) Close-up on corner (M3).

Figure 3.3: Mesh M1 and M3.

The minimum cell size ("element size" in FLUENT) have been set equal to

1×10^{-2} m. In the span-wise direction, where the width is $B = 1.8$ m, this give 180 cells. Normal to the wall, the minimum distance to the first grid point is 4.0×10^{-3} m for M1 and M2 and 3.5×10^{-3} m for M3 and M4, which is 0.22% and 0.19% of the width. The cell size on the surface of the cube have been kept constant for all meshes. This was done both in order to be able to run the simulation with the same time step for all cases and to be able to control the maximum amount of cells within a reasonable limit. Reducing the cell size on the surface was tried, but the required time step was then too low to be economical with respect to computational time needed.

Figure 3.3 show details of mesh M1 and M3, which have a cell growth rate of 10%. Figure 3.3a show how the finer mesh have been extended into the wake area in order to capture the behaviour of the wake (this is holds for all meshes). From Figure 3.3b and 3.3c it is seen how the mesh is refined close to the cube for mesh M1, while Figure 3.3d and 3.3e show this for mesh M3. From Figure 3.3c, one can see how sharp corners may create skewed cells in the inflation layer (the inner layer) and in the transition region.

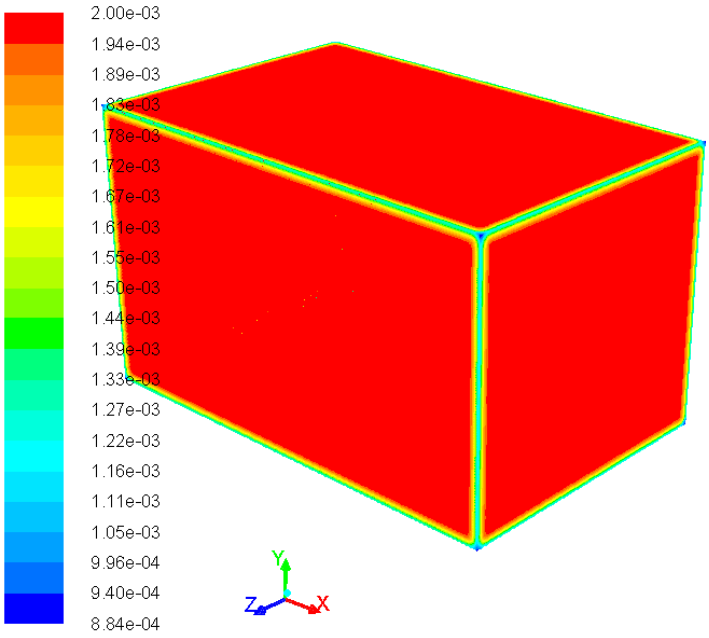

Figure 3.4: Cell-wall distance [m] for mesh M1.

From Figure 3.4 it is seen how the cell-wall distance on the cube surface

varies. It is seen that it is constant on the faces and gets smaller close to the edges and corners. The cell-wall distance is defined as the distance from the surface to the cell centroid.

For the case with the ROV simplified as a cube, the cube have been made both with sharp and rounded corners. This is because the sharp corners will induce a high local value of y^+ due to the high shear velocity. However, as seen from Figure 3.4, the cell-wall distance is less around the corners and edges. This may actually counteract the effect of high shear velocity and thus avoiding high values of y^+.

3.1.5 Test Run

In order to make sure that the CFL-condition is fulfilled (see Section 2.3.1) and to make sure that the first grid point is within the log-law region ($30 \leq y^+ \leq 200$), a bit trial and error is needed. This is done by running the simulation for a short while and observing the trend of the results.

As briefly described above, the value of y^+ may for the case of the sharp edged cube be quite high due to the high shear velocities as explained. Hence, the simulation is tried with both sharp and rounded corners. For the cube with rounded edges and corners, circular arches with radius 0.1 m are used. The results after the test runs can be seen in Table 3.1. In the table, y^+ is an area weighted average value at the last time step and Δy is the distance from the surface to the first grid point. It should be mentioned that the values for y^+ and C_D in the table are *not* the stable values. The flow is still developing and thus these will change.

Table 3.1: Test of sharp corners vs. rounded corners.

Edge type	Mesh	#Nodes	#Cells	Δy	y^+	C_D
Sharp	M1	7.08×10^6	6.75×10^6	4.0×10^{-3} m	57.9	1.69
	M2	8.10×10^6	7.75×10^6	4.0×10^{-3} m	58.6	1.69
Rounded	M3	6.86×10^6	6.54×10^6	3.5×10^{-3} m	56.4	0.11
	M4	7.84×10^6	7.51×10^6	3.5×10^{-3} m	57.4	0.11

One concern that arises for the case with a sharp edged cube, apart from the high shear velocity, is the possible high skewness of the cells around the edges and corners. This is due to the difficulties in modeling the sharp

edges numerically. Especially the transition regions from inflation mesh to regular mesh showed to be problematic (cf. Figure 3.3c on page 26). Here, highly skewed cells were not possible to avoid.

The simulations are run using a time step of $\Delta t = 0.001\,\mathrm{s}$ for two hours and thus the values of y^+ and C_D are expected to change from the values given in Table 3.1 as mentioned. The drag coefficient given in the table, is the instantaneous value after the test run is complete, i.e. for the last time step.

Based on Table 3.1 it is seen that the cube with rounded corners and edges have less nodes than the sharp edged cube. This is due to the fact that the mesh is not completely hex dominant. Around the corners, there have been created tetrahedrons due to the geometry. It is also seen that the distance from the surface to the first node can be smaller for the case with rounded corners and edges. This is as discussed due to the lower shear velocity around the corners compared with the case of sharp edges and corners.

The largest difference between the two cases is seen in the drag coefficient. As given in Section 1.4, the target range for the mean drag coefficient in 2D should be $1.07 - 2.4$ [13, 21, 29] (The results from Schewe [21] have been found in Ahlborn, Seto, and Noack [1]). It is however expected that the value for C_D for the 3D case should be smaller than C_D for the 2D case (as shown by e.g. Tian et al. [27]). This is because the flow in the 3D case also can pass around the cube on the top and bottom sides, compared with the 2D case where the flow only can pass around the sides. As seen, the drag coefficient obtained for meshes M1 and M2 are within the 2D interval, but it is expected to decrease as the flow stabilizes.

It is seen that the drag coefficient for the case with rounded edges and corners are much lower than the case with sharp edges and corners. This clearly seems like a non-physical result, but the trend for C_D is actually increasing for both M3 and M4.

3.2 Simulation of Flow Around a Fully Submerged Stationary Cube

Numerical simulation of flow around a fully submerged stationary cube with both sharp and rounded edges and corners have been performed. As observed during the test run, the initial drag coefficient obtained for the rounded cube was much lower than the sharp cube. Further study was

thus performed in order to study the flow around the rounded cube, which is important since the ROV have rounded edges. All the results have been obtained for a fully developed and stable flow.

In order to make sure that the flow is fully developed and stable, a gliding average procedure can be applied. The idea is that when fully developed the flow will have a mean value on which the time dependent quantities will fluctuate. If then several windows in a time series have almost the same time averaged value, the flow can be characterized as fully developed and stable. Several windows can thus be made e.g. in the time series of the drag coefficient C_D, each overlapping half of the next window length. The data for developing flow, which is characterized by large fluctuations, are disregarded in such an analysis.

3.2.1 Grid Convergence Study

In order to be sure that the solution is grid independent, a grid convergence study have been performed with one additional grid per case with a finer resolution (mesh M2 and M4). Ideally, this convergence study should have been performed with three or four grids per case, but due to limited available time and the great computational costs associated with 3D simulations, only two grids per case were created. The time step used for all cases was $\Delta t = 0.001$. All the time series of the force coefficients and power spectral analysis can be found in Appendix E.

Sharp Edged Cube

Table 3.2 show the results from the grid convergence study for the sharp edged cube.

Table 3.2: Grid convergence study for sharp edged cube. $\overline{C_D}$ is averaged over the last quarter of the time series.

Mesh	# Nodes	# Cells	$\overline{C_D}$	C_{Lrms}	St	y^+
M1	7.08×10^6	6.75×10^6	0.8367	0.0495	0.1132	23
M2	8.10×10^6	7.75×10^6	0.8192	0.0473	0.1132	23

From Table 3.2 and Figure 3.5 it is seen that there is good agreement for the root mean square of the lift and the mean drag coefficient (-4.4% for

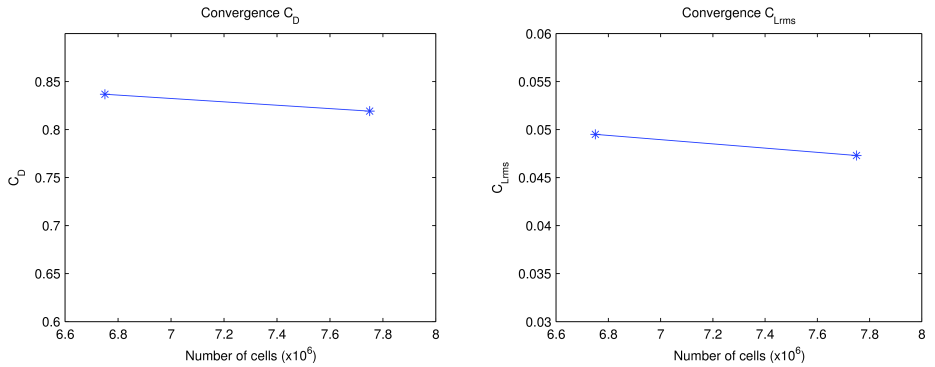

(a) C_D. **(b)** C_{Lrms}.

Figure 3.5: Grid convergence for meshes M1 and M2.

C_{Lrms} and -2.1% $\overline{C_D}$ for refinement of mesh M1). Further, the Strouhal number have been found to be identical for the two cases.

Looking at the value of y^+ for mesh M1 and M2, one see that it is a bit too low. Ideally it should have been higher than 30 - which is the boundary for the log-law region. However, y^+ is an area-weighted average value and thus the local y^+ will have both lower and higher values at different places on the cube depending on the local shear velocity.

In order to check the influence of the low y^+, a new mesh was made based on M1 where the distance from the surface to the first node was increased. This increase led to $y^+ \approx 27$. The drag coefficient was then averaged over a time interval and compared with the value from the same time interval for mesh M1. The improved version of mesh M1 gave $\overline{C_D} = 0.8331$ compared with $\overline{C_D} = 0.8348$ for M1 (averaged over the interval $50\,\text{s} \leq t \leq 140\,\text{s}$). Based on this, it was concluded that the results were good and the effect of the low y^+ could be disregarded.

Round Edged Cube

In spite of the apparent increase of the drag coefficient as commented for the test run earlier in this report, the first results for $\overline{C_D}$ for mesh M3 and M4 were still much lower (about four times) than the results obtained for the sharp edged cube (M1 and M2 cf. Table 3.2). The results also showed that the lift behaviour seemed non-physical, with a mean lift coefficient $\overline{C_L}$

smaller than zero. For this reason, and knowing that the $k-\omega$ SST turbulence model may have difficulties predicting the lift for a circular cylinder [17] (in contrast to a square cylinder - as seen by Tian et al. [26]), the decision was made to stop the simulation at $t = 50\,\mathrm{s}$, and continue using DES in conjunction with the realizable $k-\varepsilon$ turbulence model by Shih et al. [22] (details can be found in Appendix C.1).

However, the realizable $k-\varepsilon$ model showed no noticeable increase in the drag coefficient. As one can see from Figure C.2 in Appendix C, the separation occurs at the trailing edges of the cube and not the leading edges as for the sharp edged cube. For this reason, the Reynolds number was reduced to $Re = 5000$ by reducing the viscosity (run using the $k-\omega$ SST model, see Appendix C.2). This gave vortex shedding from the leading edges and an increase in the drag coefficient by approximately three times. The simulation was then yet again stopped and the Reynolds number was increased back to its original value. This resulted in a reduction in the drag coefficient and the separation point moved downstream to the trailing edges. The simulation was run for as long as possible and the results can be seen in Table 3.3. Complete time series of drag and lift coefficients plus the power spectral density of the lift can be found in Appendix E.2.

Table 3.3: Grid convergence study for round edged cube. $\overline{C_D}$ is averaged over the last quarter of the time series.

Mesh	# Nodes	# Cells	$\overline{C_D}$	C_{Lrms}	St	y^+
M3	6.86×10^6	6.54×10^6	0.2176	0.0086	0.02220	30
M4	7.84×10^6	7.51×10^6	0.2257	0.0357	0.02914	30

Figure 3.6 show that there is good agreement for the drag coefficient between meshes M3 and M4. Larger discrepancy is seen on the Strouhal number and the root mean square lift coefficient. The results clearly indicate that the lift is not very accurately predicted for the rounded cube, leading to the large difference in the root mean square of the lift coefficient for mesh M3 and M4. Looking at the fluctuations of the lift for meshes M3 and M4 (cf. Figure E.2c and E.2d in Appendix E.2), it is seen that the reason most likely is too short time series in both cases. The time series for the fluctuating lift coefficients show that it takes quite a while for the flow to begin to stabilize after being run on low Reynolds number (approximately at $t = 270\,\mathrm{s}$ and $t = 250\,\mathrm{s}$ for M3 and M4, respectively). Another reason for the poor results

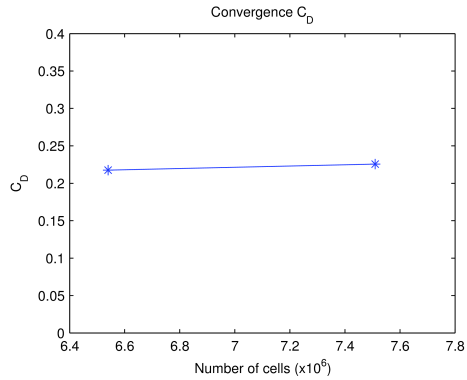

(a) C_D.

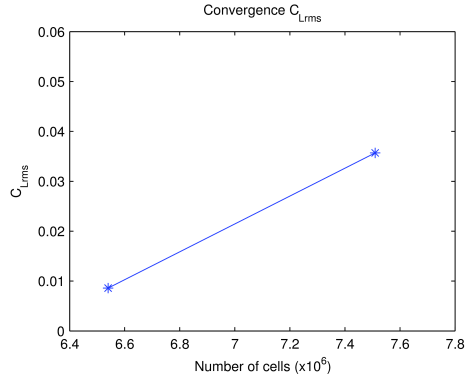

(b) C_{Lrms}.

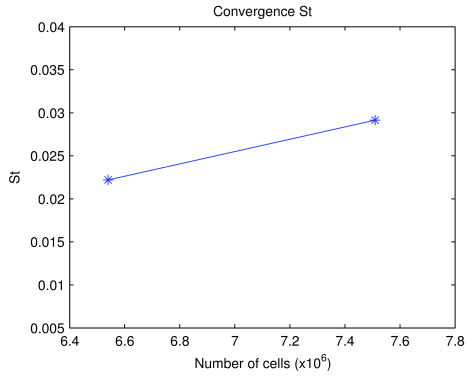

(c) St.

Figure 3.6: Grid convergence for meshes M3 and M4.

for the lift could be insufficient mesh around the edges and corners of the cube. Since the separation points are not fixed as for the sharp edged cube, further mesh refinement, especially around the edges and corners, would be preferred.

Having run the simulation at low Reynolds number ($Re = 5000$) and seen that the vortex shedding at the leading edges almost disappears for increasing Re, the low drag coefficient obtained in Table 3.3 for $Re = 8.5 \times 10^5$ can be considered to be correct. This will be further discussed in the next section.

3.3 Discussion of Results

Ideally, the convergence study should have been performed with more than two meshes per case and there should also have been performed a time step convergence study. Due to high computational demand and limited available time for calculations, this have not been performed.

3.3.1 Drag Coefficient

According to "Applied Fluid Dynamics Handbook" page 335 by Blevins [4], the drag coefficient of a square rod parallel to an incoming flow should take a value in the range $0.87 \leq C_D \leq 1.25$ depending on the relation L/D. Here, L is the length of the rod, which correspond to the length of the current cube, and D is the width and height. This means that the reference area for calculation of the force coefficients is D^2. The C_D-range is for $Re = 1.7 \times 10^5$.

Using the data for the current cube, $L = 2.8\,\text{m}$ and $D = H = 1.7\,\text{m}$, the relation $L/D = 1.65$ then give that the drag coefficient for the sharp edged cube should be between 0.87 and 0.97. However, the current Reynolds number is five times higher than the reference Reynolds number and thus a deviation from this reference value is expected. Table 3.2 show that the results for $\overline{C_D}$ obtained for the sharp edged cube agree well with Blevins [4]. A Strouhal number of $St = 0.1132$ is also in good agreement with $St = 0.12$ as given by Blevins [4] on page 313. Tian et al. [27] showed however that the Strouhal number in 3D was slightly higher than the 2D value ($St = 0.155$). In spite of this, the present results show that mesh M1 and M2 are well suited for simulating the flow around the sharp edged cube.

Also the effect of rounded edges is discussed by Blevins [4]. He states that just a rounding of 2.5% of the width of a rectangle can cause a $10 - 20\%$ reduction of the drag. For a given 2D rectangular cross-section with Reynolds number in excess of 10^4, he states that the drag coefficient is $C_D = 1.6$ (cf. Figure 2.1 on page 10), provided that the flow is fully separated from the sharp-edged nose. If the same cross-section is made with rounded corners, he states that the drag coefficient is $C_D = 0.4$. Which is only 25% of the sharp edged rectangle! He explains the lower drag for the rounded sections by three factors; a drop in the net pressure drag, rounded edges can cause postponed boundary layer separation and hence a more narrow wake leads to less drag.

Tian et al. [27] investigated the difference between 2D and 3D simulations for the flow normal to a flat plate at $Re = 1.5 \times 10^5$. He showed that the mean drag coefficient and the mean recirculation length was over-predicted by a factor of two in the 2D case. The mean recirculation length was defined as the streamwise distance from the center of the plate to the position where the mean streamwise velocity changes its sign from negative to positive. He concluded that although the geometry was nominally 2D, the 3D effects for blunt geometries should be further explored.

Now looking at Table 3.3 on page 32, the results obtained for the mean drag coefficient for meshes M3 and M4 actually agree well with Blevins [4]. The mean drag coefficient obtained for M3 and M4 are approximately 25% of the results obtained for the sharp edged cube using meshes M1 and M2. It is also seen that the mean drag coefficient for both the rounded edged cube and the sharp edged cube are about half the value for the 2D case described by Blevins [4] (as seen from Figure 2.1 on page 10). This is in good agreement with the difference noticed by Tian et al. [27]. Based on this it can be concluded that the results for the drag coefficient for both cubes agree very well with the stated reference values.

3.3.2 Flow in the Wake of the Cubes

Figure 3.7 on page 37 show the velocity profiles both streamwise through the domain and in the wake region for meshes M1, M2, M3 and M4. The streamwise velocity (Figure 3.7a and 3.7b) is taken along the X-axis at $Y = Z = 0$. Figure 3.7c and 3.7d show the streamwise velocity component along the Z-axis at $X = 1.5\,\mathrm{m}$. These figures show that this velocity component is negative in the wake close to the cube - which is expected. These figures

also show that there is good agreement between meshes M1 and M2 and M3 and M4. The last two figures (3.7e and 3.7f) show the w-component along the same line as the previous two figures. Here, larger discrepancies are seen between meshes M1 and M2, while meshes M3 and M4 show good agreement. One reason for this may be the fact that the sharp edged cube (M1 and M2) have vortex shedding from the leading edges and that this leads to a much more complex wake.

The recirculation length (L_w/H) is seen from Figure 3.7a and 3.7b as the distance from the center of the cube to the point where the streamwise velocity changes its sign from negative to positive. The plots show that there is good agreement between meshes M1 and M2 ($L_w/H \approx 1.58$ for both), while there are discrepancies between meshes M3 and M4 ($L_w/H \approx 1.79$ and $L_w/H \approx 1.22$ for M3 and M4, respectively). Both cases (sharp and round edges) show a lower recirculation length compared with Tian et al. [27]'s result of $\overline{(L_w/H)} = 2.28$. This could be due to the fact that Tian et al. [27]'s 3D simulations were for an infinitely long cylinder, i.e. the flow could only pass over and under the cylinder and *not* around the sides as for the present cubes.

The plots have been made at $t = 180\,\mathrm{s}$, when the maximum fluctuation of the lift coefficient coincide for mesh M1 and M2 and for M3 and M4.

3.3.3 Vorticity

Figure 3.8 on page 38 show vortex structures plotted on an iso-surface using $\lambda_2 = -0.082\,\mathrm{s}^{-2}$ for the sharp edged cube and $\lambda_2 = -0.135\,\mathrm{s}^{-2}$ for the round edged cube (see Appendix D for details regarding this method). From Figure 3.8a it may seem like the shedding from the sharp edged cube is much more chaotic than the round edged cube in Figure 3.8b. However, using the lift history for meshes M3 and M4 (Figure E.2c and E.2d in Appendix E) it is seen that it is difficult to obtain a dominating shedding frequency, meaning that the shedding is more random than what is the case for the sharp edged cube. Longer time series for the lift history in these two cases would thus be preferred. Figure 3.8b show that there is some shedding remaining from the leading edge after the Reynolds number was increased from $Re = 5000$ to $Re = 8.5 \times 10^5$. It is easily seen from the latter figure that the resulting wake is much more narrow than the sharp edged cube and hence this alone should result in a considerable reduction of the drag.

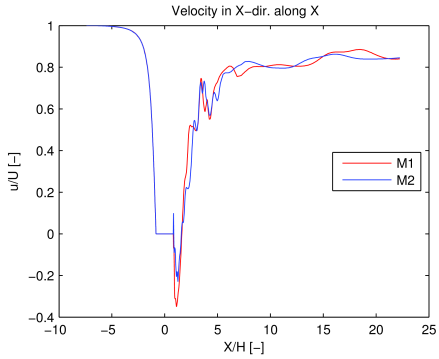

(a) u-comp. along X-axis.

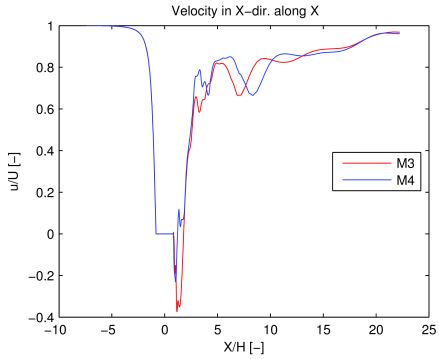

(b) u-comp. along X-axis.

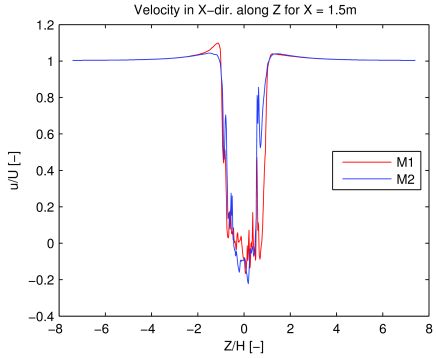

(c) u-comp. at $X = 1.5\,\mathrm{m}$.

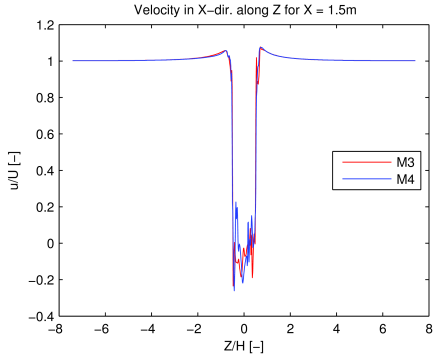

(d) u-comp. at $X = 1.5\,\mathrm{m}$.

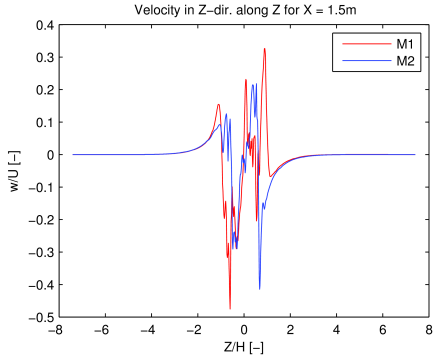

(e) w-comp. at $X = 1.5\,\mathrm{m}$.

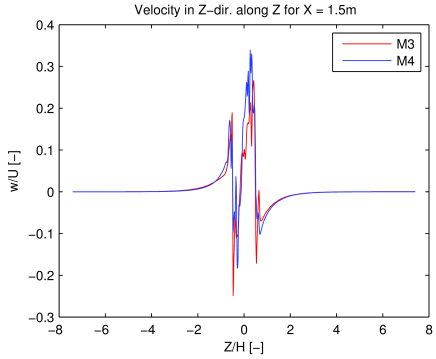

(f) w-comp. at $X = 1.5\,\mathrm{m}$.

Figure 3.7: Velocity profiles for sharp and rounded cube.

3.4 Conclusions

The flow around two fully submerged stationary cubes, both sharp edged and round edged, have been studied numerically using LES in conjunction

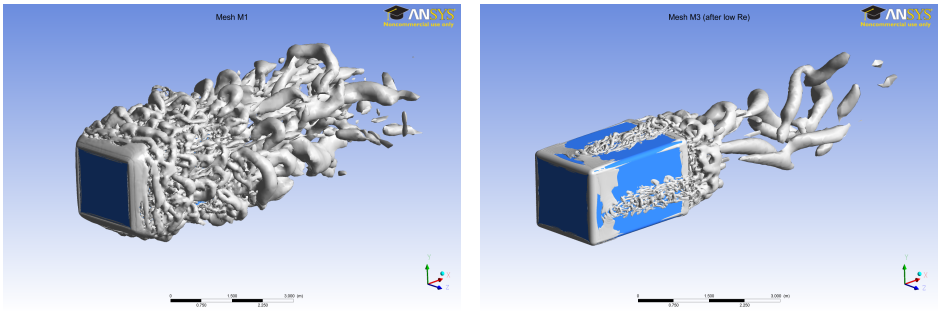

(a) M1 at $t = 250\,\mathrm{s}$. **(b)** M3 at $t = 285\,\mathrm{s}$.

Figure 3.8: Instantaneous vortical structures for meshes M1 and M3.

with the $k - \omega$ SST in the near-wall (URANS) regions at $Re = 8.5 \times 10^5$. Comparing with results stated by Blevins [4], the drag coefficients are concluded to be reasonable and in good agreement with the stated values. The lift have been shown to be more problematic to model for the cube with rounded edges. The results show that longer time series and further mesh refinement are needed in order to obtain stable mean quantities.

For the sharp edged cube, the Strouhal number have shown to be smaller than what was obtained by Tian et al. [27]. This also holds for the mean drag coefficient, which from the present study is about 40% of the reported value by [27]. This is reasonable, since the present study is of a fully submerged cube, while Tian et al. [27] studied an infinitely long cylinder (thus the flow can only pass over and under the cylinder). The mean drag coefficient obtained for the round edged cube is also considered reasonable, using results stated by Blevins [4].

At this point, it is hard to judge which of the meshes (M1 or M2 and M3 or M4) that give the most reasonable and correct hydrodynamical quantities. A further grid refinement should have been performed in order to more clearly see convergence.

Chapter 4

Merlin WR200

4.1 Modeling of Merlin WR200 ROV

In order to be able to evaluate the stability of the Merlin WR200, CFD analysis of the ROV itself is needed. However, simplifications will have to be made to the geometry. It is important that the simplified model have the same rough features as the Merlin WR200. This is necessary since the main flow behaviour around the ROV is important to model as correct as possible. If this is achieved, the instability, caused by the flow around the ROV, should be detected also in the simulation. A study of the CAD-model provided is thus a necessity.

4.1.1 Simplifying the CAD-model

There are some distinct features seen from the CAD-model which are important to model in the simplified ROV model. Firstly, there is a plate shielding some components in the aft section. This plate stretches across the entire width of the ROV and has about 60% of the height of the open tunnel which run through the ROV in the length direction. This plate clearly have a large influence on the flow passing through the ROV (Figure 4.1a and 4.1b). Secondly, there are two rectangular openings in the bottom frame of the ROV (Figure 4.1c and 4.1d). The CAD-model show that there are no components preventing the flow from passing through these holes, and thus these need to be taken into account. The top of the ROV (containing the buoyancy modules), also have similar openings, but

here the thrusters for vertical movement are located thus causing less flow to pass through. These holes will be disregarded and the top part of the ROV will be modeled in such a way that the flow is prevented from passing through. Further, it is seen that most of the components and equipment are located on the sides and in between the side columns on both sides. The side frames will thus be modeled such that no flow can pass through (Figure 4.1e and 4.1f). The rest of the internal components including the thrusters for horizontal motion and equipment in the front are disregarded (including the hydraulic arms).

As a remark, the mounting for the camera in front and the camera itself is not modeled even though these are located in the middle of the tunnel opening. This decision was made purely with regard to the mesh and mesh quality. This component clearly have some effect on the flow through the ROV, but in order to take the effect of this into account, the mesh in the tunnel of the ROV would have to have a very high resolution.

These simplifications should ensure that the main characteristics of the flow are taken into account making the model representative for flow modeling purposes and stability analysis.

4.1.2 Published Papers on the Topic

To the authors knowledge, there are to this date few published papers regarding CFD-analysis on entire ROV structures available. Gomes et al. [8] mentions that CFD of a simplified model was used to find the pressure center and hence the drag center in order to verify theoretical results. These results are however not presented in the paper. Eng et al. [6] performed a pendulum test with a scaled down model of a ROV for determining hydrodynamics coefficients. These were compared to values obtained by CFD simulations (thruster force and added mass coefficients plus linear and quadratic damping coefficients), and concluded to agree well with the experimental results. Ramirez et al. [19] used CFD simulations of an entire ROV in order to predict drag forces for design purposes. The resulting drag force was used for calculation of thruster-force. Neither [6] nor [19] give any further details regarding numerical model used in their work.

Muljowidodo et al. [16] and Valencia et al. [28] used CFD simulations of a thruster unit for numerical predictions of thruster-forces and torques. Valencia et al. [28] used the RANS equations in conjunction with both

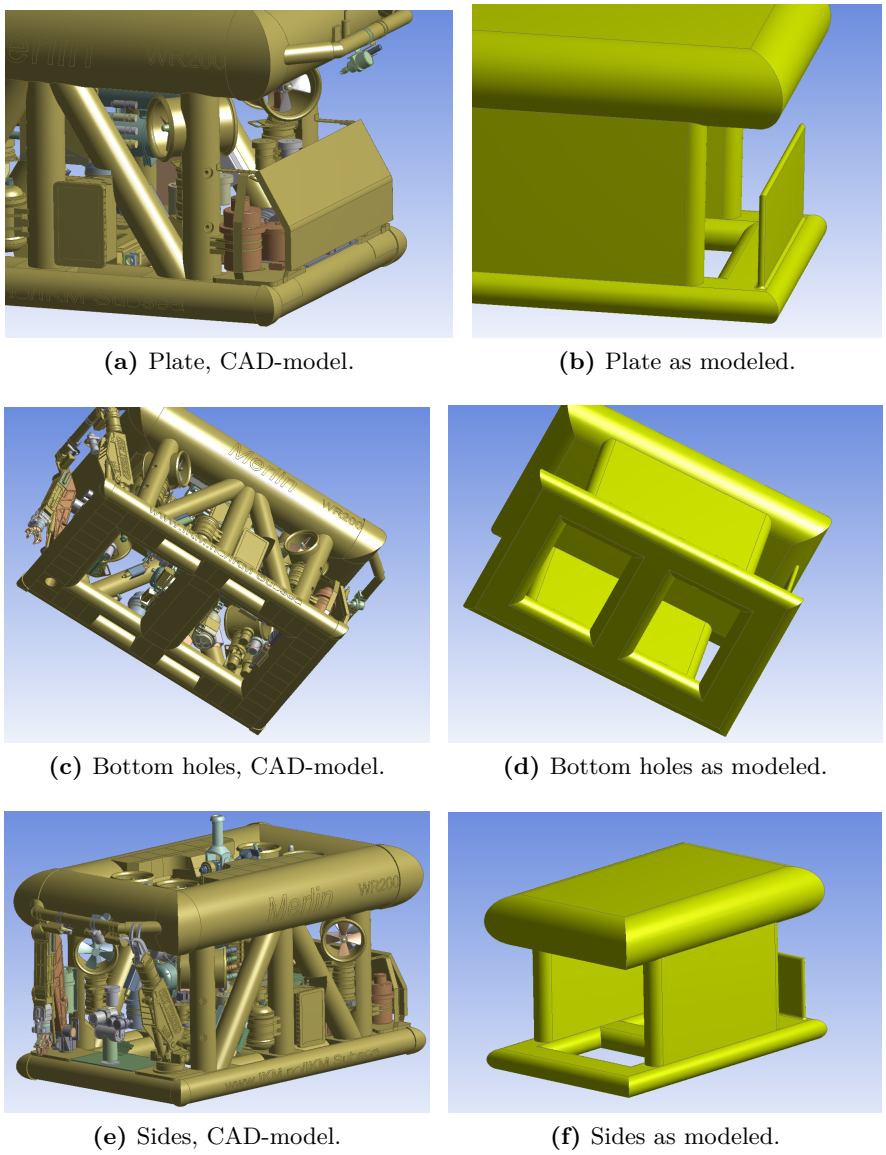

(a) Plate, CAD-model.

(b) Plate as modeled.

(c) Bottom holes, CAD-model.

(d) Bottom holes as modeled.

(e) Sides, CAD-model.

(f) Sides as modeled.

Figure 4.1: Modeled features of the ROV.

the $k - \omega$ and the Reynolds transport stresses turbulence model. They concluded that experimental tests of the thruster unit was necessary in order to be able to validate the numerical predictions. Muljowidodo et al. [16], however, combined the CFD analysis (with the RNG $k - \varepsilon$ turbulence model) with experimental tests and concluded that thruster design using

CFD methods was effective and that the approach could be used for more general cases. They reported a difference of $0 - 6.25\%$ between numerical and experimental test results.

Altogether, there seems to be no reference literature for comparison of the hydrodynamic quantities to be obtained for the simulation of the ROV. However, the same meshing technique showed very good results for the sharp edged cube. It is thus expected that the same technique should give good results also for the ROV.

4.1.3 Solver Setup

The solver used and spatial schemes are the same as used for the case of the cubes as presented earlier in this thesis (cf. Section 3.1.1), except for "momentum" where "Second Order Upwind" is used instead of "Bounded Central Differencing". Detached Eddy Simulation (DES) is used with the $k - \omega$ SST turbulence model in the near-wall URANS regions (LES in the outer regions). The numerical simulations are carried out at $Re = 8.5 \times 10^5$ and the reference values used for calculating force coefficients are:

$$\begin{aligned} A &= 2.5\,\mathrm{m}^2 \\ L &= H = 1.7\,\mathrm{m} \\ p &= 0\,\mathrm{Pa} \\ \rho &= 1025\,\mathrm{kg/m}^3 \\ \nu &= 1 \times 10^{-6}\,\mathrm{m}^2/\mathrm{s} \end{aligned} \tag{4.1}$$

For the instability analysis, the moment coefficient (C_M) is calculated about the Z-axis through the Center of Gravity (COG). This have been given by IKM Ocean Design and is located at (in current co-ordinate system):

$$\begin{aligned} X &= 53.788\,\mathrm{mm} \\ Y &= 1.156\,\mathrm{mm} \\ Z &= -6.548\,\mathrm{mm} \end{aligned} \tag{4.2}$$

The current co-ordinate system is defined with the origin at the center of the ROV, with X being positive downstream and Y positive upwards. It is thus seen that the center of gravity is located slightly starboard and aft of the origin.

Figure 4.2 show the simplified ROV from the front and aft. It is seen that the projected area is smaller than for the cube, hence the drag is expected to

be less than for the cube. It is also seen that the plate in the aft must have a large influence on the flow through the ROV. A high-pressure area on the upstream side is expected due to stagnation of the flow, while a negative pressure area is expected behind the plate. It is possible that the openings in the bottom frame are designed in order to also direct flow through and thus minimizing the maximum pressure on the plate (apart from the fact that they are needed when thrusting vertically). This might then lead to low pressure regions over or under the plate. The effect of this can be studied by plotting streamlines through the ROV and thus visualize the flow behaviour.

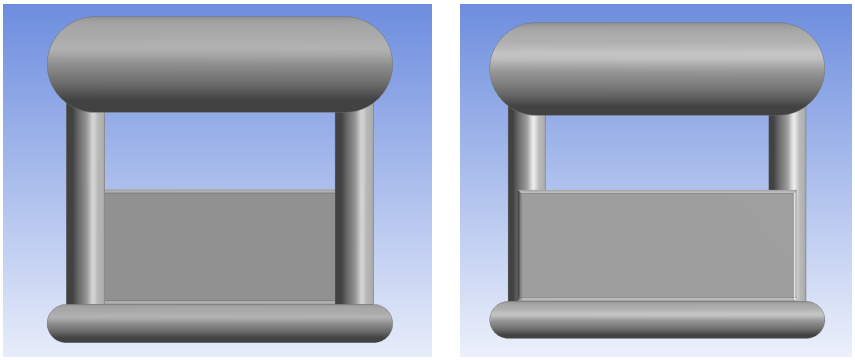

(a) Frontview. **(b)** Backview.

Figure 4.2: Frontview and backview of the simplified ROV.

4.1.4 Computational Domain and Boundaries

The computational domain can be seen in Figure 4.3a and is the same as used for the simulations of the cubes (Figure 3.1b on page 23). With B being the width of the ROV, the domain span $14B \times 14B \times 28B$. The same configuration of two smaller domains around the ROV (cf. Figure 4.3b) is also used in this case. This is necessary in order to control the sizing of the cells around the ROV - especially in the wake region. Dividing the domain stretching into the wake was done in order to assure that the cell size was approximately constant in the wake close to the ROV.

The boundary and initial conditions are also the same as used for the cubes (cf. Section 3.1.3). This involves “symmetry” boundary for the top, bottom and sides of the domain, “velocity-inlet” boundary for the inlet and “pressure-outlet” for the outlet. The ROV itself is defined as “wall”,

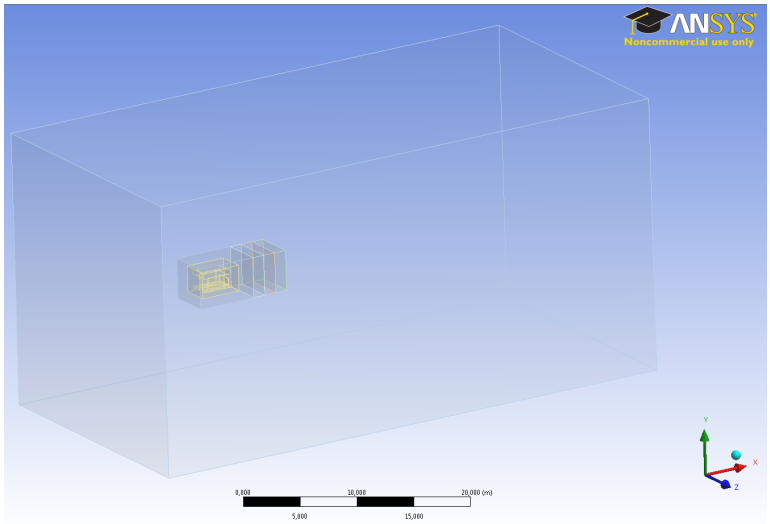

(a) Whole domain.

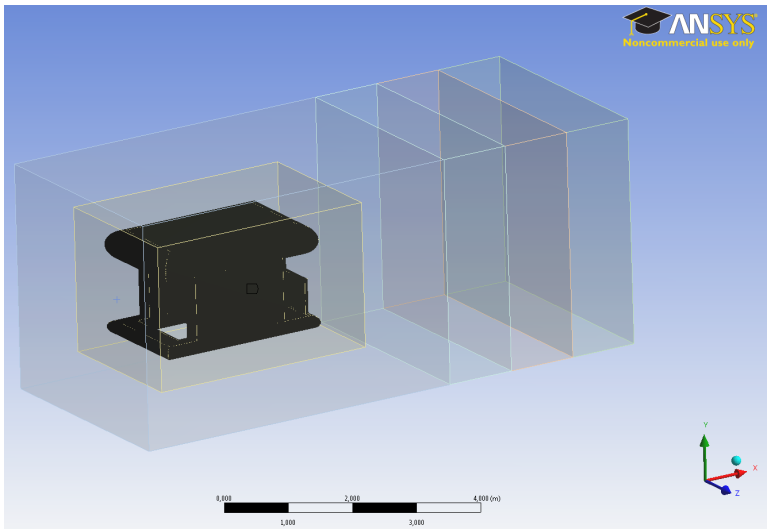

(b) Inner domains.

Figure 4.3: Domain for ROV (identical for all meshes).

i.e. the no-slip condition is valid on the surface. A turbulent intensity of 0.8% and a turbulent length of $0.0045H = 0.007\,65\,\text{m}$ is used (H being the height of the ROV).

4.1.5 Mesh

In order to keep the maximum amount of cells within a reasonable limit, some simplifications, as described in Section 4.1.1, were needed. Preferably the maximum amount of cells should not exceed eight million. This limit is based on both the available computational power and time. The latter case is regarded as decisive, since the supercomputer "Njord" is scheduled for decommissioning during the Master thesis period. This thus create a high demand on the computational resources during the final period.

As for the cubes, the ROV is meshed using the CutCell method. The results obtained for the cubes showed that this method gave good results combined with a low cell count. Face sizing is used to keep cell size constant on any given face of the geometry or inner domain faces. The minimum face size is 1×10^{-2} m - which is for all faces on the surface of the ROV. The mesh then expand with a user defined growth rate. An inflation layer has been created in order to properly resolve the boundary layer. The distance from the surface to the first node is specified as $\Delta y = 0.0045$ m - which is a bit higher than what was used for the cube. This is done in order to make sure that y^+ is within the log-law region. A total of 8 layers are used for the inflation layer (6 for the most coarse mesh). Figure 4.4 show the domain in the XY-plane and a close-up on the ROV itself (in the same plane).

Mesh Quality

Due to the more complex geometry of the ROV, good mesh quality may be difficult to achieve. Highly skewed cells were observed after the first mesh was created (mesh R2). The main problem area was identified to be the corners and edges of the plate in the aft section (especially around the base), which span across the width of the ROV. For this reason, the edges of this plate were made round with a radius of 0.02 m (the thickness of the plate being 0.04 m). Figure 4.5 show a cut through the plate in the aft of the ROV in the XY-plane. It is seen from Figure 4.5b how this effort improved the mesh in the base area (marked by red circles). This resulted in a much lower maximum aspect ratio and only a few cells exceeding a skewness of 0.98. For the refined mesh (R3), the number of highly skewed cells were reduced to 5. Still, it is also seen that the transition area from the inflation mesh to the rest of the mesh at the top of the plate is not optimal.

Other regions where bad cells may occur, are the areas where the sides meet

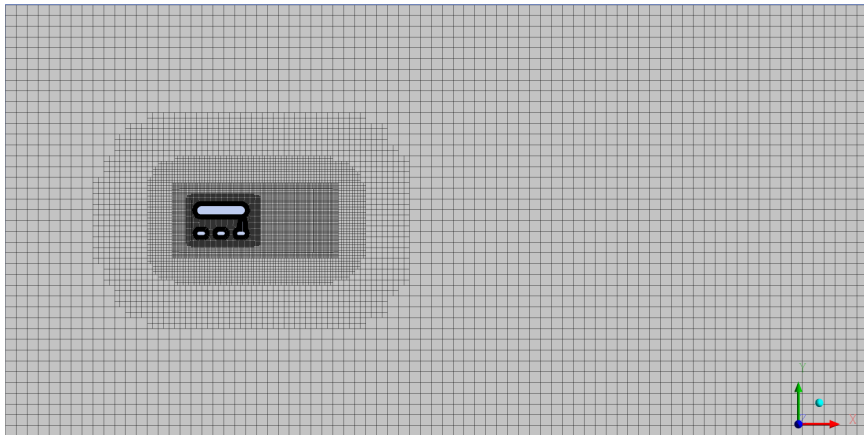

(a) Entire domain for ROV.

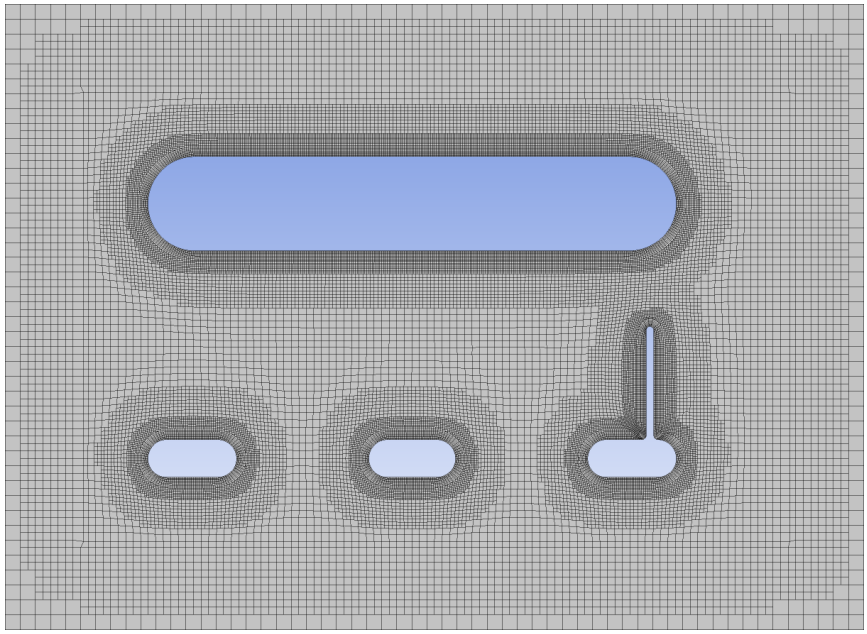

(b) Close-up on ROV.

Figure 4.4: Mesh R2 for ROV (XY-plane).

the top and bottom frame and in the corners of the openings in the bottom frame. In Figure 4.6 some of these regions are seen marked by red circles. However, the effort made by rounding the edges on the plate in the aft showed to have the largest influence on the amount of bad cells. No further effort was thus made for improving the areas as shown in Figure 4.6.

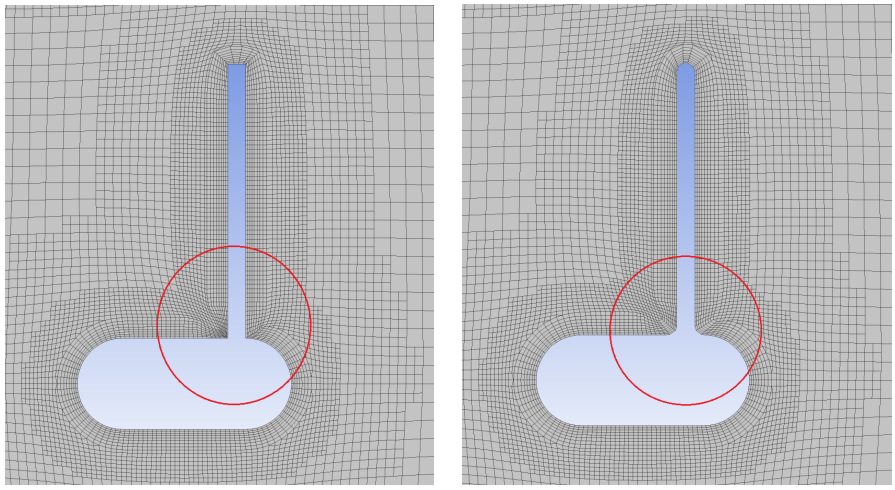

(a) Sharp edges. **(b)** Rounded edges.

Figure 4.5: Effect of rounded edges on back plate (mesh R2).

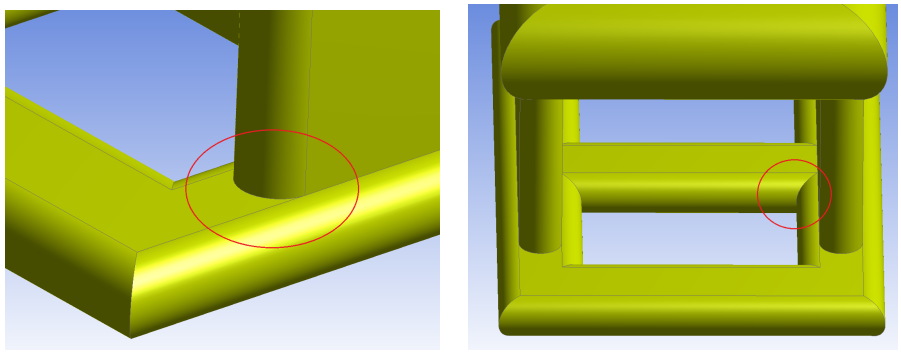

(a) Transition from bottom frame to sides. **(b)** Bottom frame openings.

Figure 4.6: Regions where skewed cells may occur.

4.2 Numerical Simulation of Flow Around Simplified Model of ROV

Numerical simulation of the flow around a simplified model of an ROV have been performed. As previously mentioned, the supercomputer "Njord" was shut down during the Master's Thesis period. This meant that only one case for the simplified ROV was planned (mesh R2). However, another opportunity for running on a local cluster ("Kongull") for high performance

computing made it possible for running two more cases for the ROV (R1 and R3). Hence, a grid convergence study for the ROV was possible.

4.2.1 Grid Convergence Study

For the grid convergence study, one coarse and one fine mesh was created. The grid size on the surface of the ROV was kept constant for all meshes since this showed to have the largest effect on the total cell count. Also the distance from the surface to the first node (in any direction) was kept constant at $\Delta y = 0.0045\,\text{m}$ resulting in $y^+ \approx 45$. The growth rates used were 10%, 10% and 8.5% for R1, R2 and R3, respectively. The element size on the inner domains were both increased and decreased in order to see the effect of a fine grid resolution versus a more coarse grid resolution in the near-surface and wake regions. For all cases, a time step of $\Delta t = 0.001\,\text{s}$ were used. This is small enough to fulfill the requirement of a Courant number less than unity.

Since mesh R2 already had been run, and a stable flow had been achieved, the data for p, ω, k, u, v and w was interpolated onto the finer mesh (R3) and the more coarse mesh (R1). The interpolation was done by FLUENT using zeroth-order interpolation. Table 4.1 show the results for meshes R1, R2 and R3. The moment coefficient (C_M) is calculated about the Z-axis through COG, which is positive on the port side of the ROV. This means that C_M corresponds to a positive pitch moment. The time series for the meshes used for the ROV can be found in Appendix E.3.

Table 4.1: Grid convergence study for ROV. $\overline{C_D}$ and $\overline{C_M}$ are averaged over the last quarter of the time series for mesh R2 and between $5\,\text{s} \leq t \leq 30\,\text{s}$ for R1 and R3.

Mesh	$\#Nodes$	$\#Cells$	$\overline{C_D}$	C_{Lrms}	$\overline{C_M}$	y^+
R1	6.71×10^6	6.34×10^6	0.5354	0.1785	-0.2579	45
R2	7.63×10^6	7.26×10^6	0.5251	0.1882	-0.2428	45
R3	8.47×10^6	8.09×10^6	0.5431	0.1778	-0.2563	45

In Figure 4.7 on page 50 the results from the grid convergence study as presented in Table 4.1 are seen. It is seen that coarsening the initial mesh (R2) gave a slight increase in both the mean drag and moment coefficient (+2% and +6.2%). This trend also holds for the refined mesh (R3) with an

increase of +3.4% and +5.6% for $\overline{C_D}$ and $\overline{C_M}$, respectively. The opposite effect is seen on the root mean square lift coefficient. The decrease for the coarse mesh (R1) is −5.2% and −5.5% for the refined mesh (R3).

Figure 4.7 show that a further refinement of mesh R3 plus a time step convergence study would have been preferred in order to see more clearly the trend of the convergence. However, due to limited available computational resources, only three meshes were possible to run. In spite of this, the overall difference between the results for the different meshes are relatively small (between 2% and 6.2%) - hence large discrepancies for further mesh refinement is not expected. The stability of the Merlin WR200 ROV will be further discussed based on the results obtained for the refined mesh R3.

4.3 Discussion of Results

The previous section show that there is good agreement between the three meshes for the force coefficients. More details in the flow around the ROV and the wake will now be discussed. All the plots from FLUENT are available as electronic appendix (due to the difficulties reading the legend).

4.3.1 Force Coefficients

Looking at the drag coefficient obtained, it is seen that it lies in between the results for the sharp edged cube and the round edged cube. Comparing with the sharp edged cube, this is reasonable since the projected area is less for the ROV. The corners of the top and bottom frame of the ROV are sharp, which is in contrast to the rounded cube which also have rounded corners. A wider wake for the ROV will thus lead to higher drag than the rounded cube. Based on this, the drag coefficients presented in Table 4.1 can be considered reasonable.

For the round edged cube, the lift was shown to be hard to model. The reason for this was concluded to be insufficient mesh around the rounded edges and corners combined with too short time series. For the ROV, the meshes show good agreement for the root mean square lift coefficient and the resulting moment - in spite of the rounded edges of the top and bottom frame. The reason for this is that the separation points for this more complex model are more or less fixed to the areas with abrupt

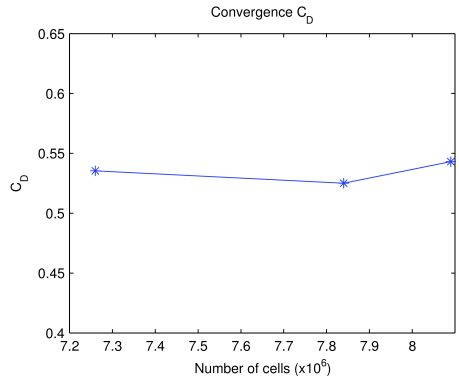

(a) C_D.

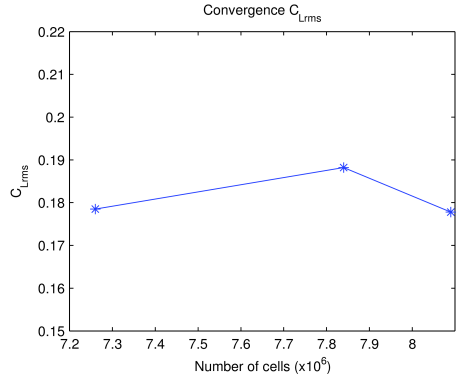

(b) C_{Lrms}.

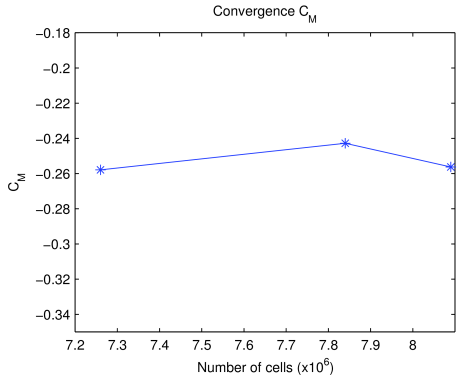

(c) C_M.

Figure 4.7: Grid convergence study for meshes R1, R2 and R3.

changes in geometry (e.g. corners of top and bottom frame, around the plate in the aft and the openings in the bottom frame).

Moment History

Figure 4.8 shows the fluctuating moment coefficient for the refined mesh R3. The peak values from the time history are $C_{M,min} = -0.2377$ and $C_{M,max} = -0.2789$. The maximum deviation from the mean value is thus 8.8%, which is quite significant! The plot show that there are seven major fluctuations in 28.6 s, which correspond to a frequency of 0.245 Hz and period of 4.09 s. This frequency most likely corresponds to the shedding from the plate in the aft, which probably is the most dominant vortex shedding (this will be further discussed in Section 4.3.5). The CAD model of the Merlin WR200 show that the thrusters are located just below the top frame. Hence, the thruster force will cause a positive pitch moment (constant moment for constant speed). If then the fluctuating negative pitch moment is combined with the constant positive thrust moment, it is clear that also the resultant moment will fluctuate significantly, leading to a pitching motion of the ROV.

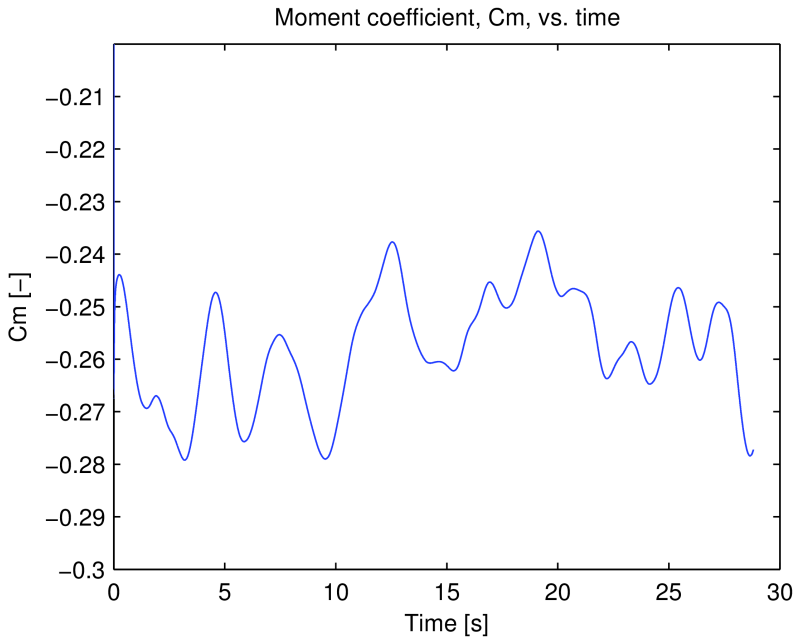

Figure 4.8: Fluctuation of the moment coefficient.

4.3.2 Velocities

Figure 4.9 show iso-surfaces of the u-component of the velocity around the ROV. The cyan color represent negative values (less than $-0.01\,\mathrm{m/s}$) while the yellow colour represent velocities higher than the inflow velocity (more than $0.53\,\mathrm{m/s}$). The figure indicates that there is a low-pressure region on the forward part of the top frame and under the bottom frame furthest to the aft. Figure 4.10a show how the u-velocity varies in the XY-plane. Here these high-velocity areas can be seen by the red colouring of the contour. The figure shows that there is a lack of symmetry in the u-velocity about the X-axis. The high-velocity area under the ROV is seen to occur further aft than the high-velocity area on the top. The reason for this is that some of the flow through the ROV is re-directed under the plate through the aft opening. The strong red colouring of the contour plot in this area supports this fact. For the top frame of the ROV, the high velocity is due to the flow being forced either over or under the frame.

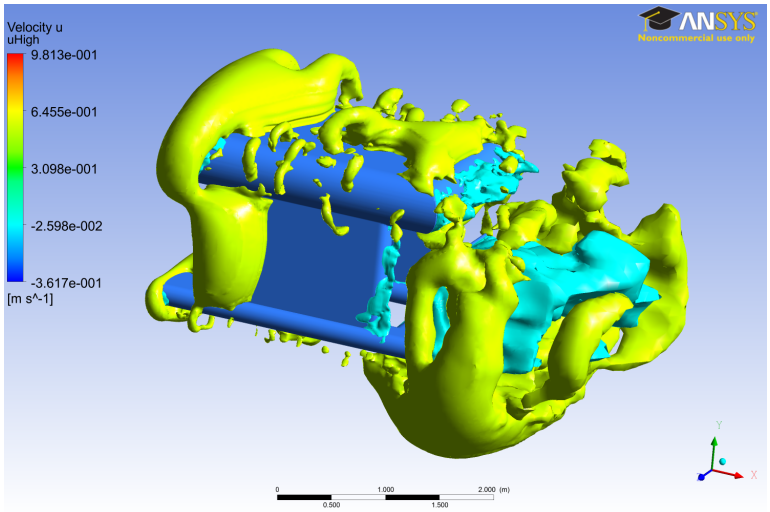

Figure 4.9: Iso-surfaces of u-velocity.

Figure 4.10b shows the v-velocity in the XY-plane. Negative velocities are shown with darker green and blue colours. Similarly, high velocity regions are recognised by yellow and red colour. Now looking at the areas described for the u-velocity, it is seen that high negative values of the v-velocity support that much of the flow is re-directed through the aft opening of the bottom frame.

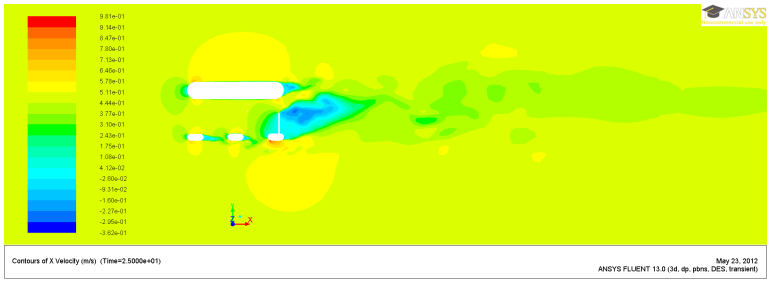

(a) u-velocity.

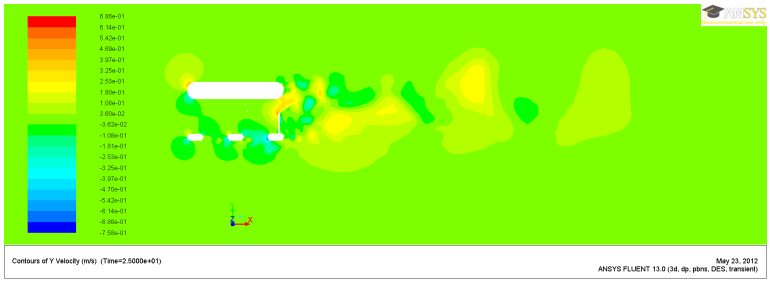

(b) v-velocity.

Figure 4.10: u- and v-component of the velocity in the XY-plane.

In Figure 4.11, streamlines through the ROV are plotted at the center ($Z = 0$). The figure indicates that there seems to be no shedding from the upstream edge of the top and bottom frame. This was also noticed for the rounded cube case. Blevins [4] explained that rounding of the edges on a rectangular section could cause postponed boundary layer separation, which is seen her by the separation occurring from the downstream edge. This figure also indicates that there is more flow through the aft opening in the bottom frame than through the forward opening. This results in the lack of symmetry in the u-velocity as seen in Figure 4.10a.

4.3.3 Pressure Distribution

Figure 4.12a show the distribution of the non-dimensional pressure coefficient in the XY-plane. This figure immediately indicates a high stagnation pressure on the top frame and especially on the lower part of the plate in the aft. Low-pressure areas are seen over the top frame and under the plate in the aft. The lack of symmetry in the u-velocity in the same plane is seen to result in an asymmetric pressure distribution in the

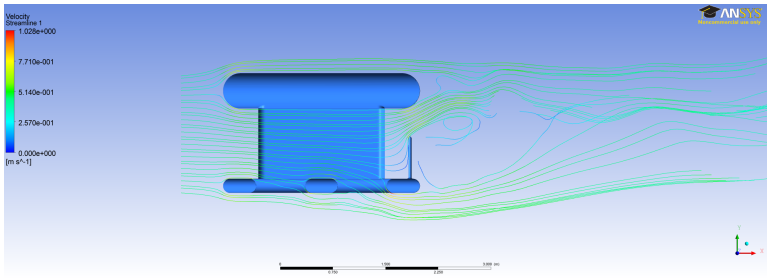

Figure 4.11: Streamlines through ROV.

same plane. If Figure 4.12a is compared with Figure 4.12b, it is seen that in the XZ-plane the pressure distribution seems more or less symmetric. From this fact it is easily understood that there should be an instability in the XY-plane. Figure 4.12b actually shows that the stagnation pressure on the plate is concentrated to the center region of the plate. This is due to the gap between the sides and the plate where the flow can escape.

(a) XY-plane.

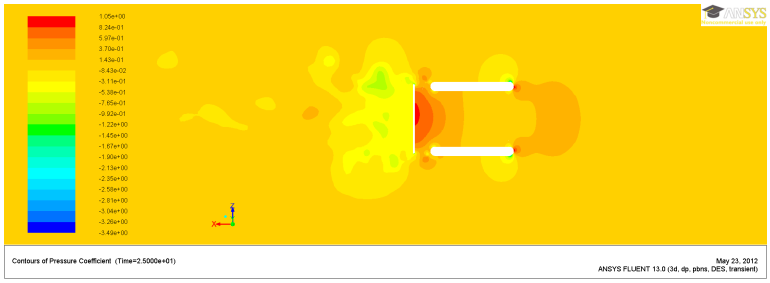

(b) XZ-plane at $Y = -0.2\,\mathrm{m}$.

Figure 4.12: C_p in the XY and XZ-plane.

The lack of symmetry in the pressure distribution is more clearly visualized

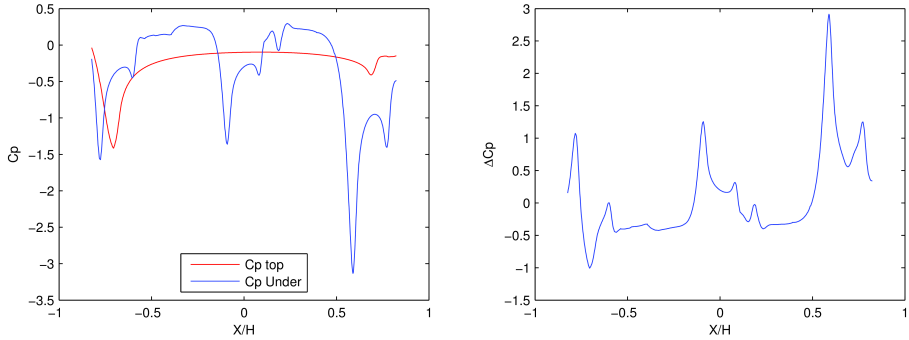

(a) Cp on top and under ROV. **(b)** ΔCp.

Figure 4.13: Cp and ΔCp for ROV.

in Figure 4.13. Here, the pressure under the bottom frame is subtracted from the pressure on the top frame of the ROV (Figure 4.13b). In Figure 4.13a the pressure on the top and under the ROV are plotted (using Cp). Initially it is seen a decrease in the pressure as the flow accelerates around the rounded edge of the top or bottom frame. The next peak for the pressure under the ROV (blue line) show where the flow accelerates around the downstream edge of the forward opening. The third and largest decrease is seen as the flow is forced through the aft opening in the bottom frame (around the downstream edge of the aft opening). Similarly, the pressure drop on top of the ROV in the aft is insignificant. Hence, the imbalance in the net pressure is clearly seen in Figure 4.13b.

The current model shows that if the plate was removed, less flow would probably flow through the aft opening leading to a more symmetric pressure distribution. However, as seen from the CAD-model previously described, there are several components placed in front of this plate, which to some extent also would prevent the flow from flowing freely through the ROV.

4.3.4 Effect of Plate

The plate in the aft of the ROV have been shown to cause a lack of symmetry in the velocity and pressure distributions in the XY-plane. However, as mentioned briefly in the previous section, the components in front of the plate might cause a similar effect as the plate. This is more clearly seen in Figure 4.14 (marked by red circles) where a cut have been

made through the ROV. Judging by this figure, these components have roughly half the height of the plate. A more accurate and detailed modeling of the ROV, including these components and disregarding the plate, would have been an interesting case to run with respect to the stability analysis and understanding of the flow behaviour. Such an analysis could perhaps give an indication to whether the plate should be removed or not and if the components in front need to be relocated. Still, since the top frame is thicker than the bottom frame, there would be a non-zero moment acting on the ROV. However, this effect may in reality be counteracted by the placement of the thrusters for horizontal movement. According to Gomes et al. [8], the ROV would not suffer from any pitch moment at constant surge velocities if the thrust vector is aligned with the resultant drag vector.

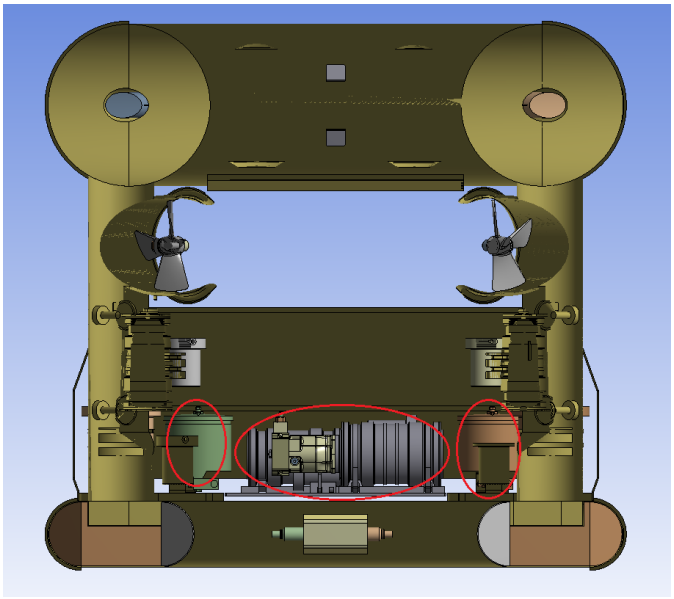

Figure 4.14: Components in front of the plate.

4.3.5 Vorticity

Figure 4.15 on page 58 shows vortex structures plotted using $\lambda_2 = -0.259\,\mathrm{s}^{-2}$. Figure 4.15a and 4.15b show that the plate generates the largest vortex structures in the wake; two from the sides, one from the top of the plate and one from the bottom frame under the plate (the last one

is more clearly seen in Figure 4.16c on page 61). These seem to interact further down the wake and causing a more randomly looking vortex pattern. In contrast to the cube with rounded edges and corners, the ROV have only rounded edges, meaning that the corners of the top and bottom frame are sharp, causing separation from all four leading corners. Looking more closely on Figure 4.15a, two major vortices are seen that have been shed from the port side of the plate (marked by red arrows). It is clearly seen from these two figures that the major vortex structures are shed from the plate, resulting in the large fluctuations seen in the moment history.

Figure 4.16 on page 61 shows the Z-vorticity in the XY-plane in different scales. The blue colour represent negative values and the red positive. Turbulent intensity in the same plane is also shown. Figure 4.16c shows more clearly that, as mentioned, the plate in the aft generates the largest vortex structures. Combined with the shedding from the top and bottom frame, the close wake looks quite chaotic. Looking at the bottom frame, it is seen that the separation from the upstream edge of the forward opening seems to prevent the flow from flowing through. The aft opening shows smaller vortices, allowing the flow to flow through. This is in consistency with what was seen from the streamlines in Figure 4.11 on page 54.

The last figure (4.16d) shows the turbulent intensity in the wake of the ROV. As expected, the turbulent intensity is high at the points where the separation occurs due to the abrupt change in the geometry. The highest intensity is seen where the vorticity from the shedding from the top frame, the plate and the bottom frame meets. Further this figure shows that the wake seems to have an oscillatory behaviour further downstream. This apparent oscillatory nature of the wake may very well be a large contributor to the instability of the ROV (as seen by the large fluctuations in the moment history). It is also recognised from the v-velocity plotted in Figure 4.10b on page 53. This figure indicates three areas of circular motion - one in the close wake and two further downstream.

Figure 4.17 on page 62 shows Y-vorticity and turbulent intensity in the XZ-plane at $Y = -0.2\,\mathrm{m}$. As previously discussed, it is seen that also here there is no vortex shedding from the forward edges of the side frame. The separation is seen to occur from the downstream edges. Scaling up the vorticity (Figure 4.17c), the wake behind the plate seems even more chaotic than what was observed in the XY-plane. The vortex structures from the downstream sides of the ROV are seen to interact with the vortex structures shed from the side of the plate on the same side.

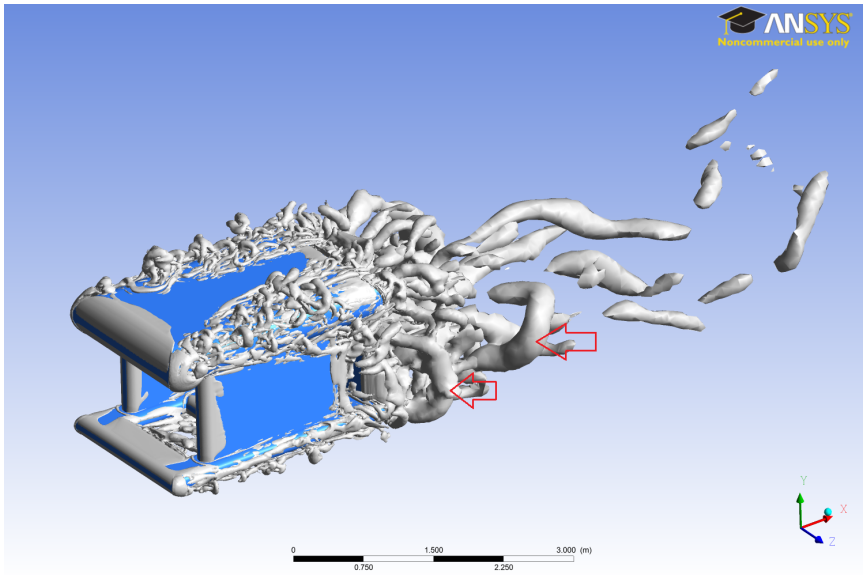

(a) Front.

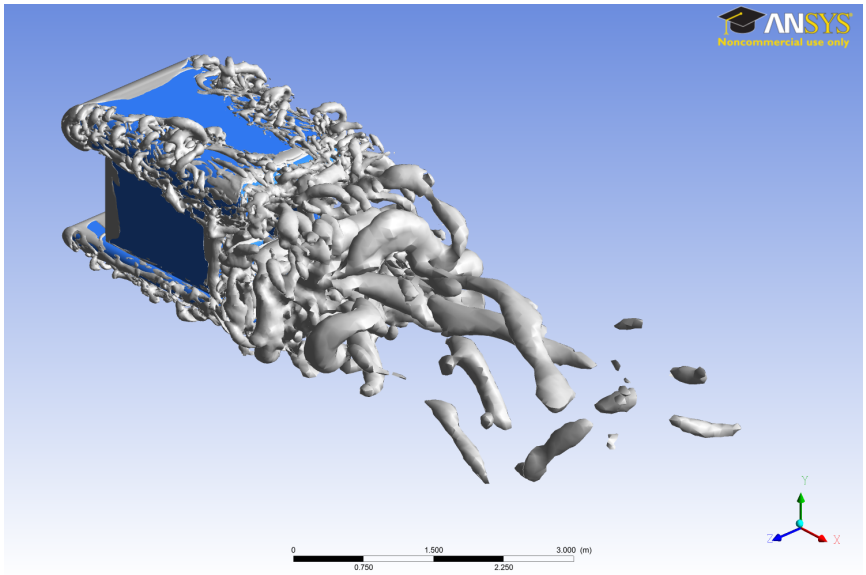

(b) Rear.

Figure 4.15: Instantaneous vortical structures for mesh R3.

Figure 4.17d show the turbulent intensity. This figure shows that the areas with the highest intensity are the areas where the vortices from the side

frame interact with the vortices from the plate side. Comparing the wake seen from this figure with Figure 4.16d, on can see that the turbulent intensity in the XZ-plane shows symmetrical features while this is clearly not the case in the XY-plane.

4.3.6 Comments Regarding the Stability of the ROV

The current simplified model of the Merlin WR200 ROV have been shown to be subjected to a non-zero mean pitch moment. As seen from Figure 4.8 on page 51, the fluctuations in the moment history are significant. During survey mode (i.e. at constant speed), the thruster force should create a constant moment. The large fluctuations in the pitch moment would then result in a pitching behaviour of the ROV, which is in good consistency with the reported instability problem. Hence, minimizing the peaks in the moment history should ensure a less violent pitching behaviour.

The first issue to be noticed is the large influence of the plate in the aft on the flow through the ROV. This plate creates a high-pressure zone in front and a negative pressure zone on the other side in the wake. The flow is seen to be forced either over the plate or under through the aft opening in the bottom frame. By studying the u-velocity and pressure distributions in the XY-plane, it is seen that there is a high-velocity region beneath the plate as a direct result of the flow-redirection, creating a low-pressure region. A similar low-pressure region is seen over the front top of the ROV which result in an asymmetric pressure distribution. As a direct result of these two low-pressures, a non-zero mean negative pitch moment is experienced by the ROV. The fluctuations in the moment have been found to arise from the shedding from the plate. The low-pressure area under the plate will vary in size during the shedding, hence causing variations in the pitch moment.

It has also been discussed that removing the plate might not be a sufficient solution due to the components placed in front. For this reason, these components could, if possible, be relocated in order to be able to remove the plate and ensuring less obstruction for the flow through the ROV. These alternatives should however first be tested numerically before any destructive action is done to the ROV.

4.4 Conclusions

The flow behaviour around and through the simplified model of the Merlin WR200 have been studied numerically at $Re = 8.5 \times 10^5$ using LES in conjunction with the $k - \omega$ SST turbulence model in the near-wall (URANS) regions. The stability is studied by means of the fluctuating moment coefficient, velocity and pressure distributions and vorticity.

The cause of the instability is concluded to be the lack of symmetry in the velocity distribution in the XY-plane, and hence also the pressure distribution. This causes a non-zero mean pitch moment. The shedding from the plate in the aft is most likely the cause of the large fluctuations seen in the moment, causing the pitching motion of the Merlin WR200.

The present results show that in order to be able to propose an effective solution to the instability of the ROV, a more detailed modeling of the components in the aft of the ROV is needed for comparison. These can then be relocated in order to ensure minimal flow obstruction through the ROV. However, based on the present results, it can be concluded that the redirection of the flow through the ROV (and thus the plate itself) probably is the major contributor to the instability of the current model.

(a) Range: $-20\,\mathrm{s}^{-1}$ to $20\,\mathrm{s}^{-1}$.

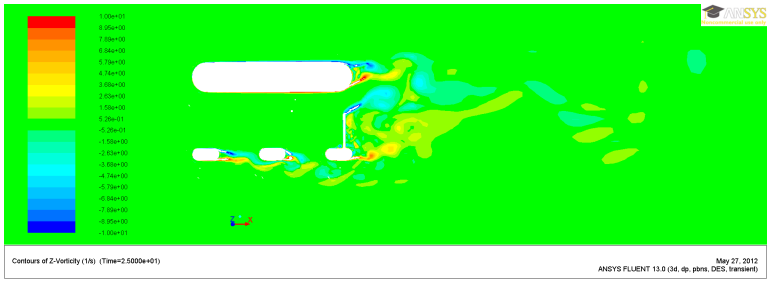

(b) Range: $-10\,\mathrm{s}^{-1}$ to $10\,\mathrm{s}^{-1}$.

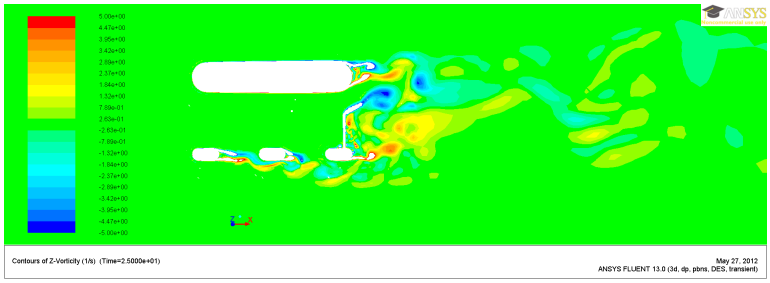

(c) Range: $-5\,\mathrm{s}^{-1}$ to $5\,\mathrm{s}^{-1}$.

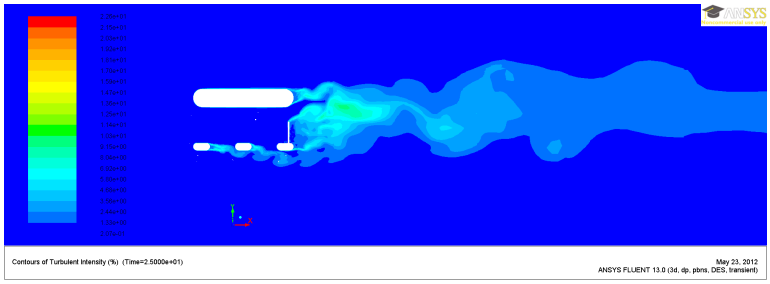

(d) Turbulent intensity (range 0.2% to 20%).

Figure 4.16: Z-vorticity and turbulent intensity in the XY-plane.

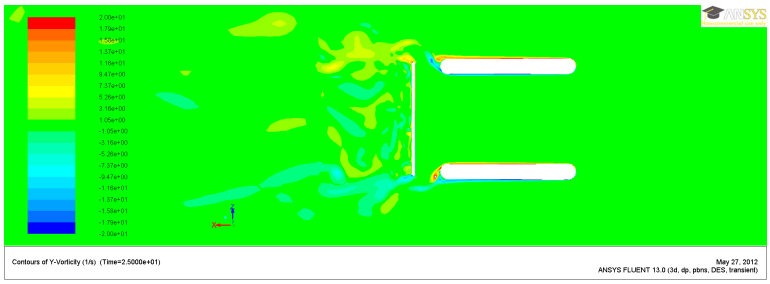

(a) Range: $-20\,\mathrm{s}^{-1}$ to $20\,\mathrm{s}^{-1}$.

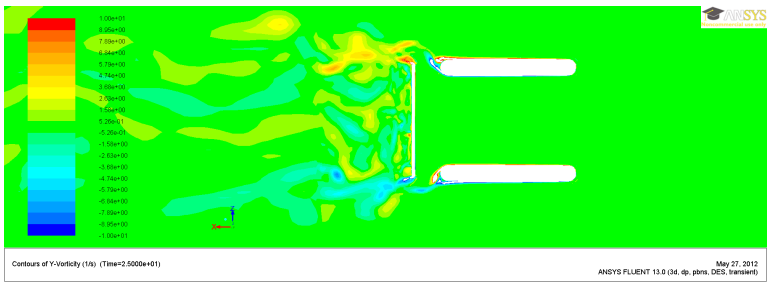

(b) Range: $-10\,\mathrm{s}^{-1}$ to $10\,\mathrm{s}^{-1}$.

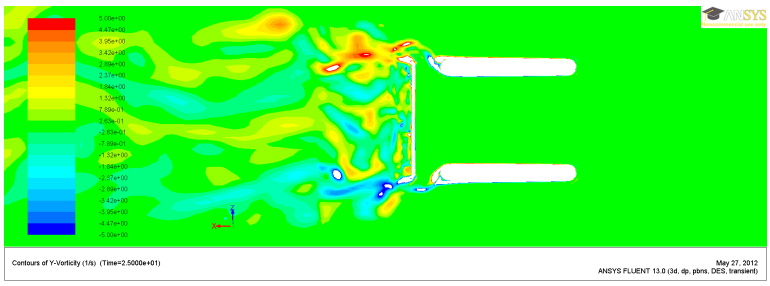

(c) Range: $-5\,\mathrm{s}^{-1}$ to $5\,\mathrm{s}^{-1}$.

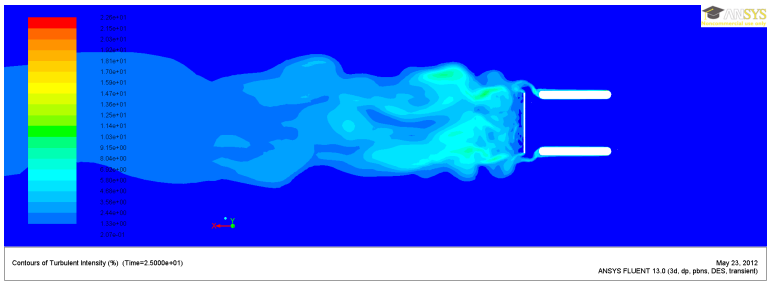

(d) Turbulent intensity (range 0.2% to 20%).

Figure 4.17: Y-vorticity and turbulent intensity in the XZ-plane at $Y = -0.2\,\mathrm{m}$.

Chapter 5

Conclusions and Recommendations for Further Work

The flow structure around the ROV "Merlin WR200" have been studied numerically at $Re = 8.5 \times 10^5$ by means of Computational Fluid Dynamics (CFD) using LES in conjunction with the $k - \omega$ SST turbulence model in the near-wall (URANS) regions.

5.1 Conclusions

As a start, the ROV was simplified as a fully submerged stationary rectangular cube, with both sharp and round edges. By studying these two cases, the effect of the rounded edges was seen to have a large influence on the hydrodynamical quantities obtained. The mean drag coefficient for the round edged case was found to be approximately 25% of the case when the rectangular cube had sharp edges. By studying published work of similar cases, the mean drag coefficient is concluded to be in good agreement with the stated values. The lift was however hard to model correct for the case with rounded edges, and it is concluded that longer time series and further mesh refinement are needed in order to get stable mean quantities. For the case with sharp edges, the lift have been shown to be more easily modeled. Very good results were obtained for all the force coefficients. The Strouhal number obtained in this case is in good agreement with published

reference values. However, due to the fact that only two meshes was used per case, it is concluded that a further mesh refinement is needed in order to more clearly see convergence of the results obtained.

Due to the good results obtained for the rectangular cubes, the same meshing technique was used for the simplified model of the Merlin WR200. Three meshes were made for the grid convergence study, the largest difference between the meshes was found to be 6.2%. Altogether, the discrepancies between the meshes are concluded to be small and the results obtained to be good. The moment coefficient history showed that there was a negative mean pitch moment acting on the ROV. The largest fluctuation was found to be 8.8% from the mean value. This fluctuating moment was identified as the reason for the pitching motion of the ROV in survey mode in surge. By means of a more detailed study of the velocity and pressure distributions in different planes, it was discovered that there was a low-pressure area on the front top of the ROV and under the the aft of the ROV. This would then clearly result in a negative pitch moment. Further, it is concluded that the main contributor to the instability of the current simplified ROV model, is the plate in the aft spanning across the width of the ROV. This plate causes some of the flow through the ROV to be forced through the aft opening in the bottom frame, creating a high-velocity region and hence the low-pressure region observed under the ROV in the aft. This low-pressure region will vary in size during the shedding process from the plate, hence causing the variations seen in the pitch moment. Based on this, it is concluded that the plate should be removed in order to not prevent the flow from flowing freely through the ROV. However, if this is done, the components in front of the plate might have to be relocated. This should be further studied numerically before any destructive action is done to the ROV.

Although there were small discrepancies between the meshes, the trend were increased results for the force coefficients both for more coarse and refining the mesh. For this reason, it is concluded that a further mesh refinement or also a time step convergence study should be applied in order to more clearly see convergence.

5.2 Recommendations for Further Work

The main contributor to the instability of the ROV, have been identified to be the plate in the aft. For this reason it would be interesting to make

an even more detailed model of the ROV, perhaps without the plate for comparison of the moment history. However, if the plate was to be removed, a study of the CAD model show that there are components in the aft that need to be taken into account. These components may actually cause a similar effect as the plate itself, and may thus have to be relocated. This would be an interesting topic of investigation for a Master's Thesis, investigating the stability of the ROV for different placements of these components. Experimental tests with a scaled model (or full size) for comparison would also be of great interest. Further, the instability in survey mode in sway have not been investigated at all. Hence, numerical simulation of the flow structure for this operating mode would also be of great interest. Altogether, the amount of remaining work could be suitable for a Doctoral Thesis.

References

[1] B. Ahlborn, M. L. Seto, and B. R. Noack. "On drag, Strouhal number and vortex-street structure". *Fluid Dynamics Research* 30.6 (2002), pp. 379 –399.

[2] ANSYS Inc. *ANSYS FLUENT Theory Guide*. Version 13.0. 2010.

[3] ANSYS Inc. *ANSYS FLUENT User Guide*. Version 13.0. 2010.

[4] R. D. Blevins. *Applied Fluid Dynamics Handbook*. Krieger Pub Co, 2003. ISBN: 157524182X.

[5] CFD Online. *Introduction to turbulence/Nature of turbulence*. [Online; accessed 31-January-2012]. 2012. URL: `http://www.cfd-online.com/Wiki/Introduction_to_turbulence/Nature_of_turbulence#What_is_turbulence.3F`.

[6] Y. Eng, W. Lau, E. Low, G. Seet, and C. Chin. "Estimation of the Hydrodynamics Coefficients of an ROV using Free Decay Pendulum Motion". *Engineering Letters* 16.3 (2008).

[7] Y. Gao and W. Chow. "Numerical studies on air flow around a cube". *Journal of Wind Engineering and Industrial Aerodynamics* 93.2 (2005), pp. 115 –135.

[8] R. Gomes, A. Martins, A. Sousa, J. Sousa, S. Fraga, and F. Pereira. "A new ROV design: issues on low drag and mechanical symmetry". *Oceans 2005 - Europe*. Vol. 2. 2005, pp. 957 –962.

[9] J. O. Hinze. *Turbulence*. 2nd ed. McGraw-Hill, 1975. ISBN: 0-07-029037-7.

[10] J. Jeong and F. Hussain. "On the Identification of a Vortex". *Journal of Fluid Mechanics* 285 (1995), pp. 69–94. DOI: `10.1017/S0022112095000462`.

[11] W. Jones and B. Launder. "The calculation of low-Reynolds-number phenomena with a two-equation model of turbulence". *International Journal of Heat and Mass Transfer* 16.6 (1973), pp. 1119 –1130.

[12] D. Lakehal and W. Rodi. “Calculation of the flow past a surface-mounted cube with two-layer turbulence models”. *Journal of Wind Engineering and Industrial Aerodynamics* 67-68.0 (1997), pp. 65 –78.

[13] B. Lee. “The effect of turbulence on the surface pressure field of a square prism”. *J. Fluid Mech.* 69.2 (1975), pp. 263 –282.

[14] F. Menter. “Two-Equation Eddy-Viscosity Turbulence Models for Engineering Applications”. 32.8 (1994). AIAA Journal, pp. 1598–1605.

[15] F. Menter, M. Kuntz, and R. Langtry. “Ten years of industrial experience with the SST turbulence model” (2003). Turbulence, Heat and Mass Transfer 4, Begell House, Inc.

[16] K. Muljowidodo, SaptoAdiN., N. Prayogo, and A. Budiyono. “Design and testing of underwater thruster for SHRIMP ROV-ITB”. *Indian Journal of Marine Sciences* 38.3 (2009), pp. 338–345.

[17] M. C. Ong, T. Utnes, L. E. Holmedal, D. Myrhaug, and B. Pettersen. “Numerical simulation of flow around a circular cylinder close to a flat seabed at high Reynolds numbers using a $k^\smile\varepsilon$ model”. *Coastal Engineering* 57.10 (2010), pp. 931 –947.

[18] D. A. Paterson and C. J. Apelt. “Simulation of flow past a cube in a turbulent boundary layer”. *Journal of Wind Engineering and Industrial Aerodynamics* 35.0 (1990), pp. 149 –176.

[19] J. A. Ramirez, R. E. Vasquez, L. B. Gutierrez, and D. A. Florez. “Mechanical/Naval design of an underwater remotely operated vehicle (ROV) for surveillance and inspection of port facilities”. *Proceedings of IMECE2007. ASME 2007 International Mechanical Engineering Congress and Exposition*. 2007.

[20] W. Rodi. “Comparison of LES and RANS calculations of the flow around bluff bodies”. *Journal of Wind Engineering and Industrial Aerodynamics* 69-71.0 (1997), pp. 55 –75.

[21] G. Schewe. *Untersuchung der aerodynamischen Kräfte, die auf stumpfe Profile bei großen Reynolds-Zahlen wirken*. Tech. rep. 84-19. Göttingen: Deutsche Forschungs- und Versuchsanstalt für Luft- und Raumfahrt, 1984.

[22] T.-H. Shih, W. W. Liou, A. Shabbir, Z. Yang, and J. Zhu. “A new $k-\varepsilon$ eddy viscosity model for high reynolds number turbulent flows”. *Computers & Fluids* 24.3 (1995), pp. 227 –238.

[23] J. Smagorinsky. “General Circulation Experiments with the Primitive Equations”. *Monthly Weather Review* 91.3 (1963), pp. 99 –164.

[24] P. Spalart, W. Jou, M. Stretlets, and S. Allmaras. “Comments on the Feasibility of LES for Wings and on the Hybrid RANS/LES

Approach". *Advances in DNS/LES, Proceedings of the First AFOSR International Conference on DNS/LES*. 1997.

[25] B. M. Sumer and J. Fredsoe. *Hydrodynamics Around Cylindrical Structures (Advanced Series on Ocean Engineering)*. World Scientific Publishing Company, 2006. ISBN: 9812700390.

[26] X. Tian, M. C. Ong, J. Yang, and D. Myrhaug. "Two-Dimensional Numerical Simulation of Flow Around Rectangular Structures With Different Aspect Ratios". *Proceedings of the ASME 2011 30th International Conference on Ocean, Offshore and Arctic Engineering*. OMAE2011-49525. 2011, pp. 395–403.

[27] X. Tian, M. C. Ong, J. Yang, D. Myrhaug, and G. Chen. "Three-dimensional effects of the flow normal to a flat plate at a high Reynolds number". *Proceedings of the ASME 2012 31st International Conference on Ocean, Offshore and Arctic Engineering*. OMAE2012-83730. 2012.

[28] R. A. Valencia, J. A. Ramirez, L. B. Gutierrez, and M. J. Garcia. "Modeling and simulation of an underwater remotely operated vehicle (ROV) for surveillance and inspection of port facilities using CFD tools". *Proceedings of the ASME 27th International Conference on Offshore Mechanics and Arctic Engineering*. OMAE2008-57459. 2008.

[29] F. M. White. *Fluid Mechanics, sixth edition (McGraw-Hill Series in Mechanical Engineenrig)*. McGraw-Hill, 2008. ISBN: 9780071286459.

[30] Wikipedia. *Law of the wall — Wikipedia, The Free Encyclopedia*. [Online; accessed 31-January-2012]. 2011. URL: `http://en.wikipedia.org/w/index.php?title=Law_of_the_wall&oldid=449155366`.

[31] Wikipedia. *Fiberglass — Wikipedia, The Free Encyclopedia*. [Online; accessed 27-January-2012]. 2012. URL: `http://en.wikipedia.org/w/index.php?title=Fiberglass&oldid=472685416`.

[32] Wikipedia. *Remotely operated underwater vehicle — Wikipedia, The Free Encyclopedia*. [Online; accessed 27-January-2012]. 2012. URL: `http://en.wikipedia.org/w/index.php?title=Remotely_operated_underwater_vehicle&oldid=473410326`.

[33] D. C. Wilcox. *Turbulence Modeling for CFD (Second Edition)*. D C W Industries, 1998.

[34] D. C. Wilcox. *Turbulence Modeling for CFD (Third Edition)*. D C W Industries, 2006. ISBN: 1928729088.

[35] A. Yakhot, H. Liu, and N. Nikitin. "Turbulent flow around a wall-mounted cube: A direct numerical simulation". *International Journal of Heat and Fluid Flow* 27.6 (2006), pp. 994 –1009.

[36] M. M. Zdravkovich. *Flow Around Circular Cylinders Volume 1: Fundamentals*. Oxford University Press, USA, 1997. ISBN: 0198563965.

[37] M. Zhao, L. Cheng, and B. Teng. "Numerical Modeling of Flow and Hydrodynamic Forces around a Piggyback Pipeline near the Seabed". *Journal of Waterway, Port, Coastal, and Ocean Engineering* 133.4 (2007), pp. 286–295.

Appendix A

Mesh Quality

A.1 Skewness

Skewness is measured between 0 and 1. Highly skewed cells should be avoided, generally up to 0.94 is acceptable while higher than 0.98 is unacceptable. There are two methods for determining cell skewness:

1. Equilateral volume deviation - applies for triangles and tetrahedrons:

$$\text{Skewness} = \frac{\text{optimal cell size} - \text{cell size}}{\text{optimal cell size}} \tag{A.1}$$

2. Normalized angle deviation - applies for all cell and face shapes:

$$\text{Skewness} = max\left[\frac{\theta_{\max} - \theta_e}{180 - \theta_e}, \frac{\theta_e - \theta_{\min}}{\theta_e}\right] \tag{A.2}$$

Here θ_e is the equiangular face/cell, i.e. 60° for triangles and tetrahedrons and 90° for quads and hexahedrons.

A.2 Orthogonal Quality

Orthogonal quality is a quantity which Ansys Fluent allow the user to check for determining mesh quality. For all faces i, the following is calculated:

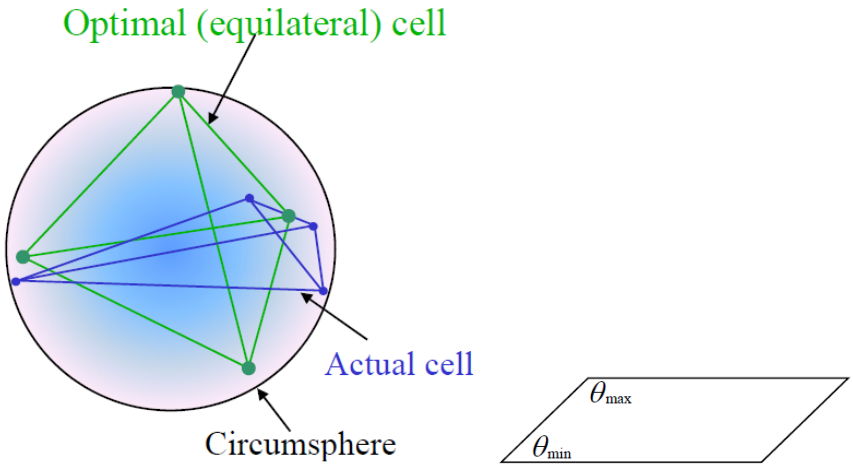

(a) Optimal cell size. **(b)** Definition of angles.

Figure A.1: Cell skewness [3].

1. The normalised dot product of the area vector of a face ($\vec{A}_i$) and a vector from the centroid of the cell to the face center ($\vec{f}_i$):

$$\frac{\vec{A}_i \cdot \vec{f}_i}{|\vec{A}_i||\vec{f}_i|} \tag{A.3}$$

2. The normalised dot product of the area vector of a face and a vector from the centroid of the cell to the centroid of the next cell sharing the same face ($\vec{c}_i$):

$$\frac{\vec{A}_i \cdot \vec{c}_i}{|\vec{A}_i||\vec{c}_i|} \tag{A.4}$$

The minimum value of these two equations are then referred to as the orthogonal quality of the cell. Values close to 0 are bad, while values close to 1 are good. For a face, the minimum value of the following is used:

$$\frac{\vec{A}_i \cdot \vec{e}_i}{|\vec{A}_i||\vec{e}_i|} \tag{A.5}$$

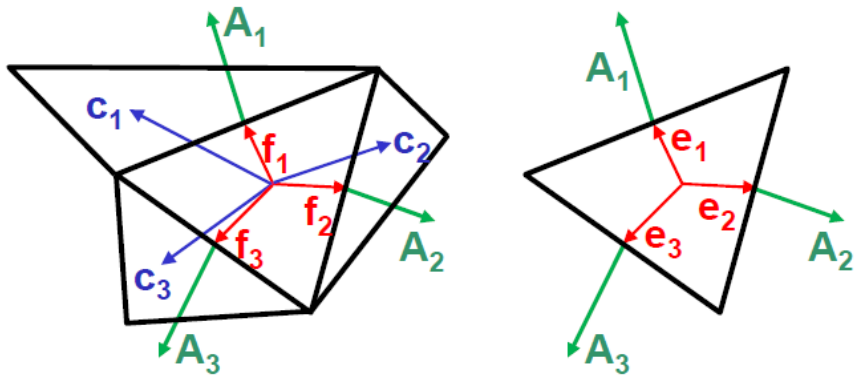

Figure A.2: Vector definition. Cells to the left, faces to the right [3].

A.3 Aspect Ratio

The aspect ratio is an important part when determining the mesh quality. Generally, it can be described as a measure of the stretching of a cell. It is computed as the ratio between the maximum and minimum value of certain distances in a given cell: distance between the cell and face centroid and the cell centroid and nodes [3]. Figure A.3 illustrates this for a unit cubical cell.

A.4 Smoothness

Rapid change in cell volume between neighbouring cells will result in large errors due to the difference between the partial derivatives in the governing equations and their discrete approximations. This is also commonly known as truncation error. A smooth mesh will not have this rapid change in cell size and hence smoothness is an important factor when evaluating mesh quality.

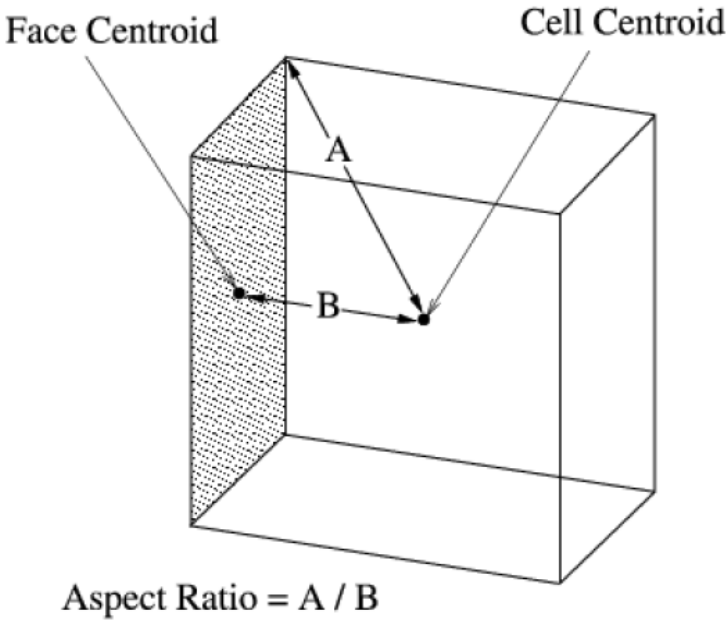

Figure A.3: Distances for a unit cubical cell [3].

Appendix B

Details in the URANS Equations

The Reynolds stress component (from Equation (2.22)) can be expressed using the Boussinesq approximation:

$$-\overline{u_i' u_j'} = \nu_t \left(\frac{\partial u_i}{\partial x_j} + \frac{\partial u_j}{\partial x_i} \right) - \frac{2}{3} k \delta_{ij} \tag{B.1}$$

Where k is the turbulent kinetic energy and δ_{ij} is the Kronecker delta, which is defined as a function of two variables or integers, being equal to 1 if they are equal and zero if not:

$$\delta_{ij} = \begin{cases} 1, & \text{if } i = j \\ 0, & \text{if } i \neq j \end{cases} \tag{B.2}$$

The turbulent kinetic eddy viscosity may then be determined as [15]:

$$\nu_t = \frac{a_1 k}{max(a_1 \omega, S F_2)} \tag{B.3}$$

Here, S is the invariant measure of the strain rate and F_2 a second blending function given as [15]:

$$F_2 = \tanh \left[max \left(2 \frac{\sqrt{k}}{0.09 \omega y}, \frac{500 \nu}{y^2 \omega} \right)^2 \right] \tag{B.4}$$

The constants used in the $k - \omega$ SST model are: $C_\mu = 0.09$, $\sigma_{k1} = 0.85034$, $\sigma_{k2} = 1$, $\sigma_{\omega 1} = 0.5$, $\sigma_{\omega 2} = 0.85616$, $\alpha_1 = 0.5532$, $\alpha_2 = 0.4403$, $\beta_1 = 0.075$, $\beta_2 = 0.0828$, $\beta^* = 0.09$, $a_1 = 0.31$ and $c_1 = 10$.

Appendix C

Troubleshooting the Rounded Cube Case

C.1 Using the Realizable $k-\varepsilon$ Turbulence Model

When simulating the flow around the fully submerged stationary cube with rounded edges and corners, it was discovered that the $k-\omega$ SST turbulence model might have difficulties in predicting both the drag and the lift. The latter case was also observed in Ong et al. [17], when comparing the root mean square lift coefficient produced by the standard $k-\varepsilon$ turbulence model on a pipe close to a flat seabed with results obtained by Zhao, Cheng, and Teng [37] using a $k-\omega$ turbulence model. However, Tian et al. [26] showed that the $k-\omega$ SST turbulence model was able to produce the lift on a 2D square cylinder very well. These two facts lead to the assumption that the rounded edges and corners might create difficulties for the $k-\omega$ SST model.

As seen from Figure C.1b and C.1d, the lift history seemed to be incorrect. The mean lift for this case would be expected to be zero, which is not the case here. Looking at the drag history in Figure C.1a and C.1c, it was seen that the flow seemed to be stable.

Figure C.2 show that the flow separates from the trailing edges instead of the leading edges (iso-surface of $\lambda_2 = -0.142\,\mathrm{s}^{-2}$). As a result of this, the wake is much more narrow and hence the drag is also much less. It was however expected that the separation should occur from the leading edges, and for this reason it was wanted to investigate if the problem could be

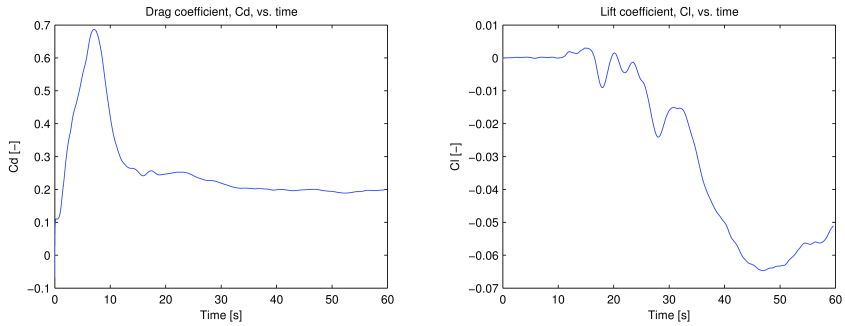

(a) C_D for M3. **(b)** C_L for M3.

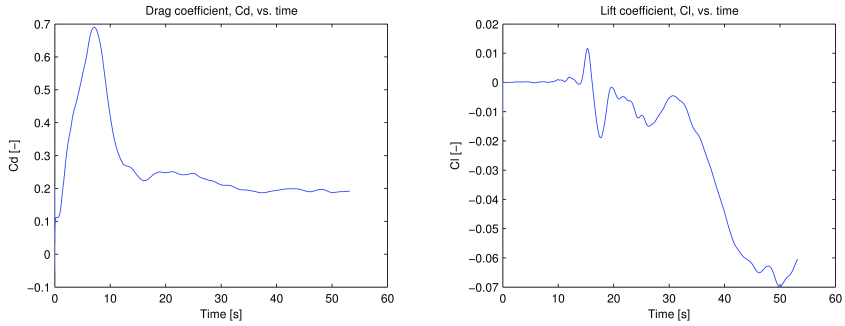

(c) C_D for M4. **(d)** C_L for M4.

Figure C.1: Drag and lift coefficients for M3 and M4 using the $k-\omega$ SST model.

the turbulence model or simply if the flow was still developing. In order to check the first possibility, the simulation was stopped and continued using the realizable $k-\varepsilon$ turbulence model by Shih et al. [22].

It is seen from Figure C.3 that the realizable $k-\varepsilon$ turbulence model did not give the desired increase in the drag coefficient. This may then indicate that the flow was still developing and that FLUENT might have too much damping in the code, which causes problems when the edges are rounded compared with sharp edges. In order to check if the shedding from the trailing edges was correct, the Reynolds number was dropped to $Re = 5000$ in order to trigger shedding from the leading edges. If then the shedding move downstream for increasing Reynolds number, the initial results for M3 and M4 could be verified.

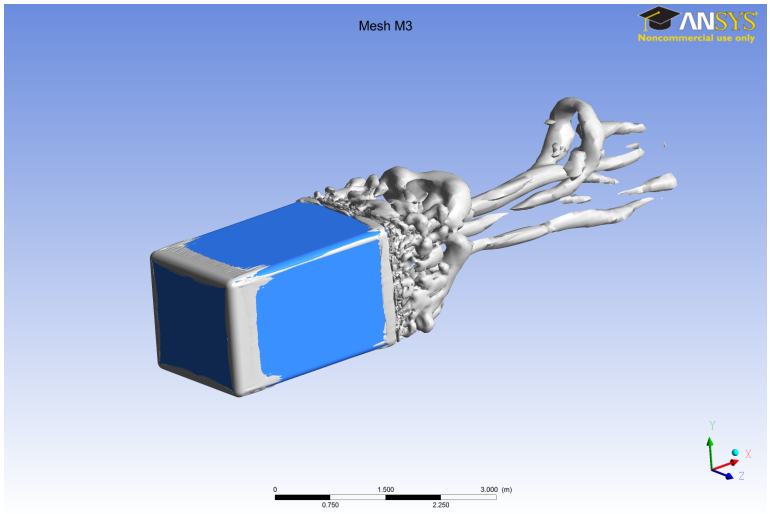

Figure C.2: λ_2 criterion at $t = 50\,\mathrm{s}$ for mesh M3.

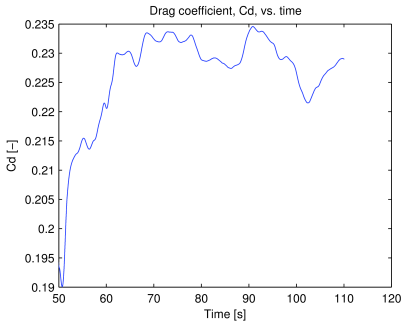

(a) C_D for M3.

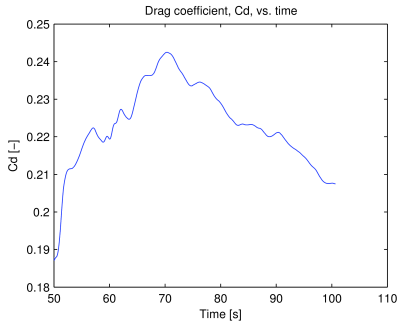

(b) C_D for M4.

Figure C.3: Time series of drag coefficient using the realizable $k - \varepsilon$ model.

C.2 Re = 5000

In Figure C.4a, instantaneous vortical structures are plotted at $t = 115\,\mathrm{s}$ using the $\lambda_2 = -0.0137\,\mathrm{s}^{-2}$. It is clearly seen that vortex shedding was achieved at the leading edges and corners. When the drag history seemed to be stable, the Reynolds number was increased to its original value. Figure C.4b show that there was still some shedding left from the leading edges, but mostly from the trailing edges. The vortices are plotted using $\lambda_2 = -0.135\,\mathrm{s}^{-2}$.

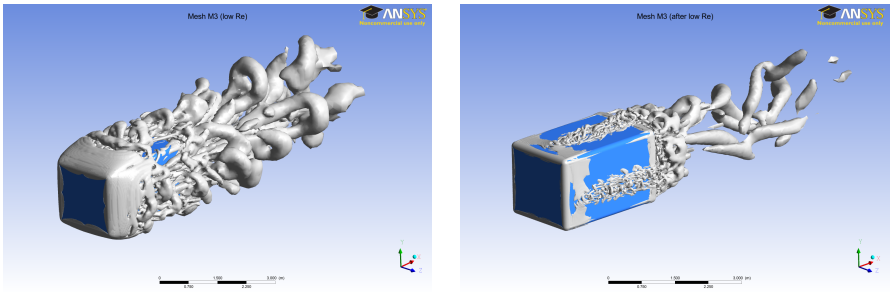

(a) $Re = 5000$. **(b)** $Re = 8.5 \times 10^5$.

Figure C.4: Iso-surfaces of λ_2 for mesh M3.

Now, looking at the time history for the drag coefficient in Figure C.5, it is seen that the mean value have increased to approximately 0.6. This is about 75% of the value for the sharp edged cube, and given that separation occurs from the leading edges this agrees well with Blevins [4]. He states that a rounding of the edges can cause a reduction of the drag by $10-20\%$. Hence, it is concluded that the low drag at $Re = 8.5 \times 10^5$ must be correct.

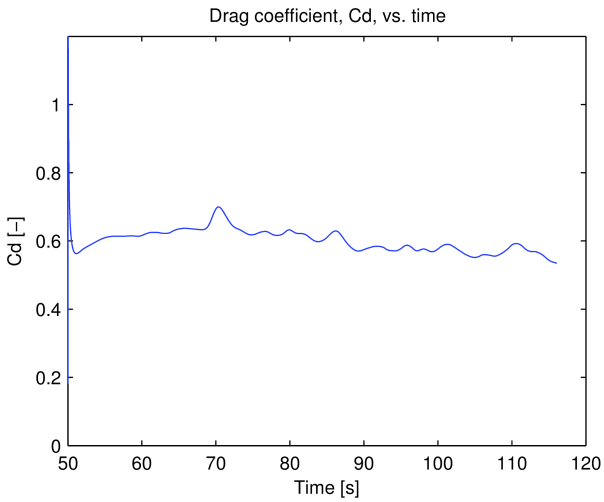

Figure C.5: C_D for M3 at $Re = 5000$.

Appendix D

λ_2 Method

The λ_2 method by Jeong and Hussain [10] is a commonly used vortex detection algorithm. Often, a pressure minimum is used to identify a vortex, but according to Jeong and Hussain [10] this pressure minimum is *not* enough as a detection criterion. The explanation is that a pressure minimum may exist without a vortex due to unsteady irrotational straining and that viscous effects may eliminate a pressure minimum within a vortex. These effects are removed by only considering the contribution from $\mathbf{S^2} + \mathbf{\Omega^2}$. Here, $\mathbf{S}$ is the symmetric component (rate of deformation or strain rate) of the velocity gradient tensor $\mathbf{J}$. $\mathbf{\Omega}$ is then the antisymmetric component (spin tensor):

$$\mathbf{S} = \frac{\mathbf{J} + \mathbf{J^T}}{2} \tag{D.1}$$

$$\mathbf{\Omega} = \frac{\mathbf{J} - \mathbf{J^T}}{2} \tag{D.2}$$

Since $\mathbf{S^2} + \mathbf{\Omega^2}$ is real and symmetric, there are only real eigenvalues (λ_1, λ_2 and λ_3). A vortex is then defined as a region where $\mathbf{S^2} + \mathbf{\Omega^2}$ has two negative eigenvalues. λ_2 is defined as the second largest eigenvalue ($\lambda_1 \geq \lambda_2 \geq \lambda_3$) and if it is negative at a point, this point belongs to a vortex core. One weakness with the λ_2 method is that it may have difficulties distinguishing between individual vortices when several vortices exist.

Here, Q is given as:

$$Q = -\frac{1}{2}(\lambda_1 + \lambda_2 + \lambda_3) \tag{D.3}$$

Table D.1: Possible choices of eigenvalues [10].

λ_1	λ_2	λ_3	$\sum \lambda_i$	Negative λ_2	Positive Q
+	−	−	−	vortex core	vortex core
+	−	−	+	vortex core	not vortex core
+	+	−	−	not vortex core	vortex core
+	+	+	+	not vortex core	not vortex core

Table D.1 show the possible combinations for the eigenvalues (taken from Jeong and Hussain [10]).

Appendix E

Force Coefficients

The force coefficients have been plotted using MATLAB. The Strouhal number is found by means of Fast Fourier Transform (FFT) of the fluctuating lift coefficient. This is because the instantaneous lift force changes sign for each vortex shedding. Hence, the dominating frequency found by means of FFT of the time series of the lift coefficient will correspond to the vortex shedding frequency (f_v). The FFT is performed in FLUENT by choosing a sufficiently long time interval ($\approx 100\,\mathrm{s}$, which corresponds to roughly 10 vortex sheddings) in the lift coefficient series.

When performing the FFT analysis, FLUENT uses a so-called prime-factor algorithm. This algorithm is known for preserving the original data better than the conventional FFT [3].

In section E.3, the time series for meshes R1 and R3 are much shorter compared with R2. This is because the stable solution of R2 was interpolated onto R1 and R3, hence long time series was not needed.

E.1 Sharp Edged Cube

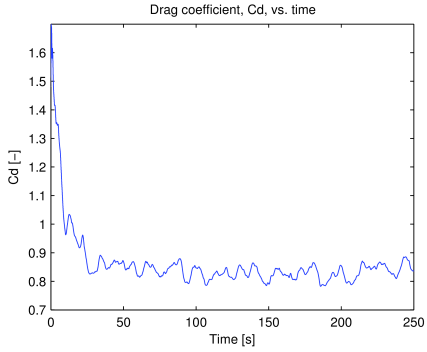

(a) C_D M1.

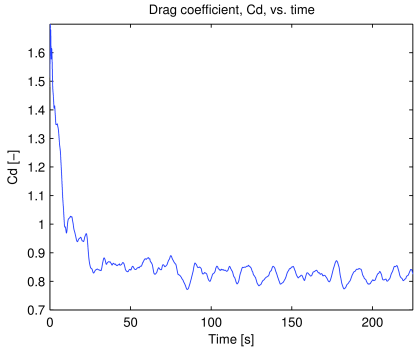

(b) C_D M2.

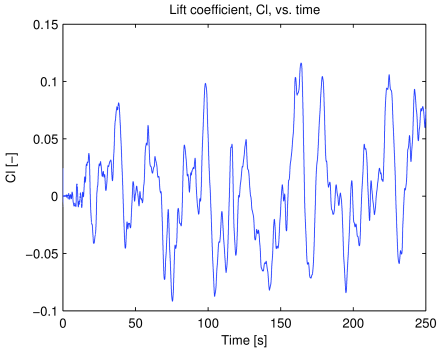

(c) C_L M1.

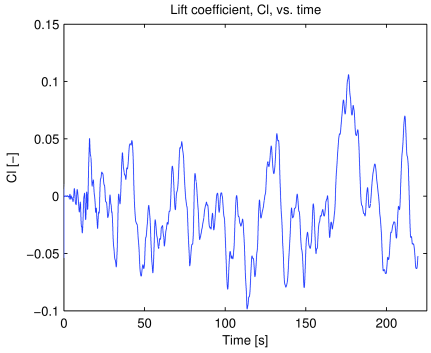

(d) C_L M2.

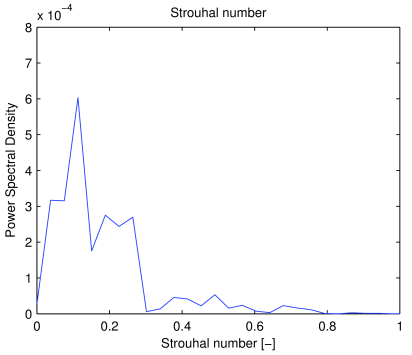

(e) St M1.

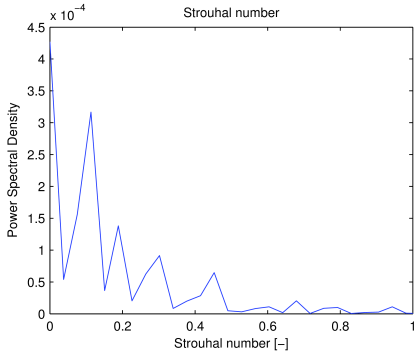

(f) St M2.

Figure E.1: Drag and lift history and power spectral density for mesh M1 and M2.

E.2 Round Edged Cube

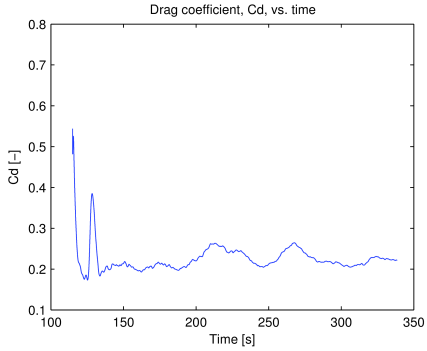

(a) C_D M3.

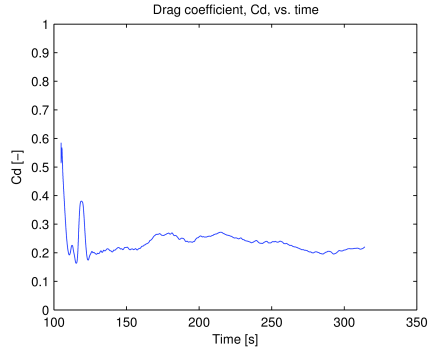

(b) C_D M4.

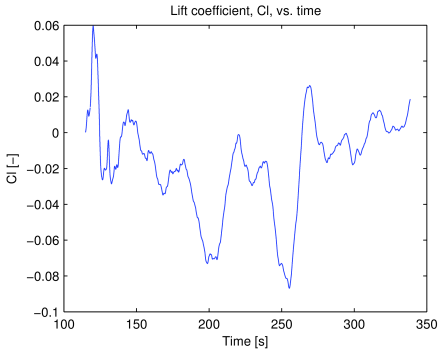

(c) C_L M3.

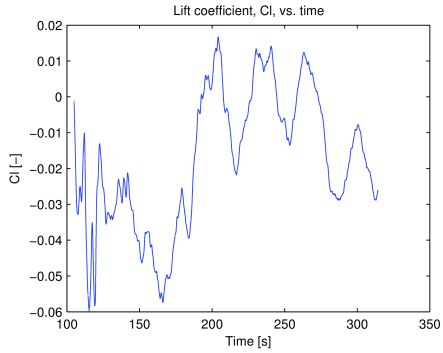

(d) C_L M4.

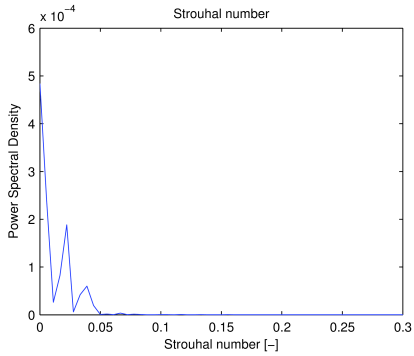

(e) St M3.

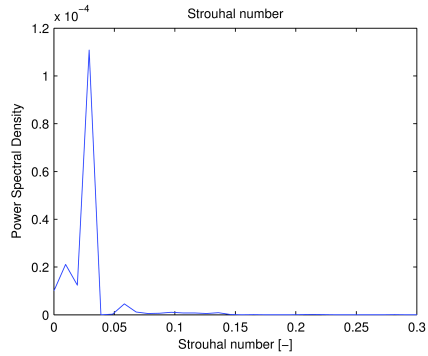

(f) St M4.

Figure E.2: Drag and lift history and power spectral density for mesh M3 and M4.

E.3 ROV

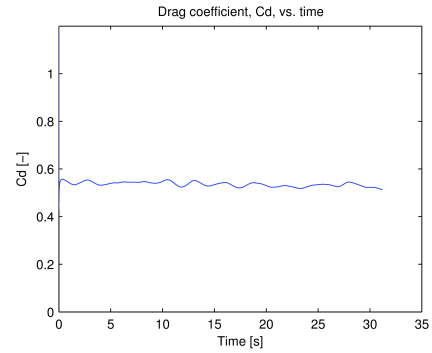

(a) C_D R1.

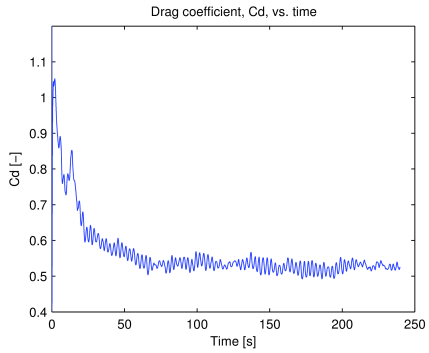

(b) C_D R2.

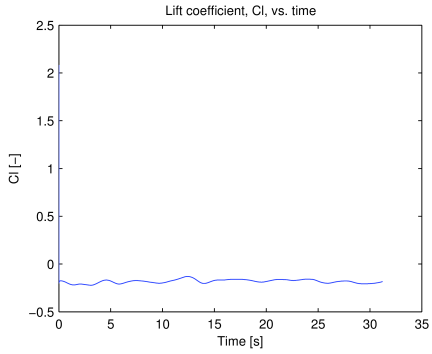

(c) C_L R1.

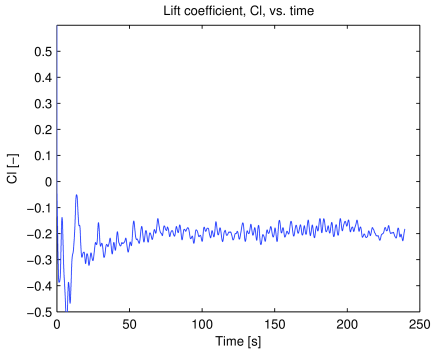

(d) C_L R2.

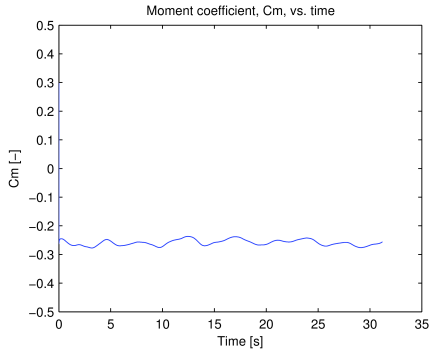

(e) C_M R1.

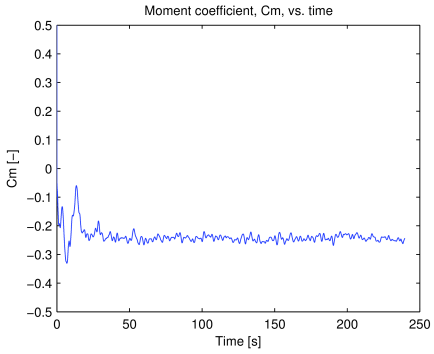

(f) C_M R2.

Figure E.3: Drag, lift and moment history for ROV (R1 and R2).

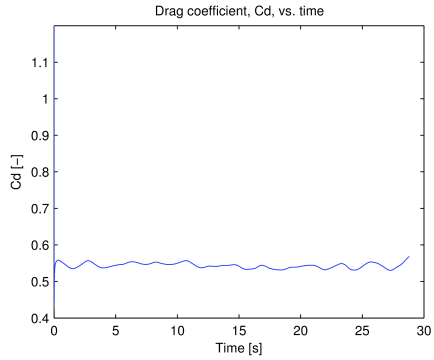

(a) C_D R3.

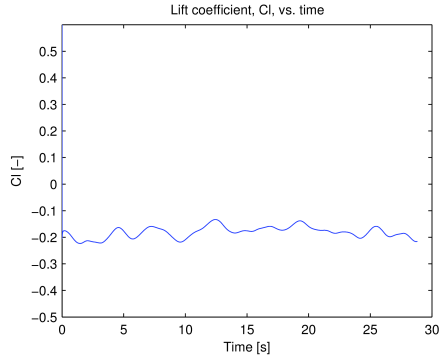

(b) C_L R3.

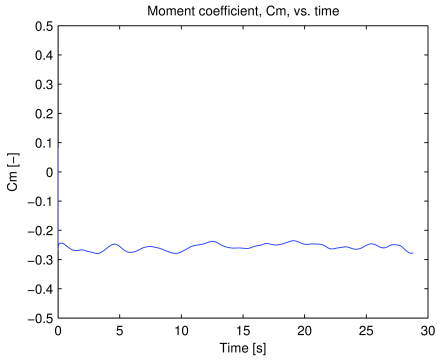

(c) C_M R3.

Figure E.4: Drag, lift and moment history for ROV (R3).